

# Nonadiabatic derivative couplings through multiple Franck-Condon modes dictate the energy gap law for near and short-wave infrared dye molecules

Pablo Ramos,<sup>1</sup> Hannah Friedman,<sup>2</sup> Cesar Garcia,<sup>2</sup> Ellen Sletten,<sup>2</sup> Justin R. Caram,<sup>2</sup> and Seogjoo J. Jang<sup>1, a)</sup>

<sup>1)</sup>Department of Chemistry and Biochemistry, Queens College, City University of New York (CUNY), 65-30 Kissena Boulevard, Queens, New York 11367, USA

<sup>§</sup>Chemistry and Physics PhD programs, CUNY Graduate Center

<sup>2)</sup>Department of Chemistry and Biochemistry, University of California, Los Angeles, Los Angeles, California 90095, United States

(Dated: 20 September 2023)

Near infrared (NIR, 700 – 1,000 nm) and short-wave infrared (SWIR, 1,000 – 2,000 nm) dye molecules exhibit significant nonradiative decay rates from the first singlet excited state to the ground state. While these trends can be empirically explained by a simple energy gap law, detailed mechanisms of the nearly universal behavior have remained unsettled for many cases. Theoretical and experimental results for two representative NIR/SWIR dye molecules reported here clarify an important mechanism of such nature. It is shown that the first derivative nonadiabatic coupling terms serve as major coupling pathways for nonadiabatic decay processes exhibiting the energy gap law behavior and that vibrational modes other than the highest frequency ones also make significant contributions to the rate. This assessment is corroborated by further theoretical comparison with possible alternative mechanisms of intersystem crossing to triplet states and also by comparison with experimental data for deuterated molecules.

Despite the utility and reliability of the Born-Oppenheimer approximation<sup>1,4</sup> in general, nonadiabatic couplings between adiabatic potential energy surfaces can be significant in some cases, playing key roles for important quantum transfer and relaxation processes.<sup>3–7</sup> Well established examples include electron and proton transfer reactions and internal conversion between excited electronic states of comparable energies, for which various theoretical and computational advances<sup>4–14</sup> have been made. On the other hand, the role of nonadiabatic derivative couplings (NDCs) as direct routes for nonradiative transitions from the first excited singlet state to the ground electronic state, has long remained unsettled. A widely held view<sup>15,16</sup> is that such direct nonadiabatic transitions are insignificant due to large energy gaps between excited and ground states. Thus, many nonradiative decay processes are hypothesized to occur going through dark forbidden states or via an activated crossing to special nonadiabatic coupling regions such as conical intersections. Indeed, there are many examples with solid experimental evidences for transitions through such indirect<sup>4,5,17</sup> or special routes,<sup>4,5,18</sup> for which advanced theoretical and computational approaches have also been developed.<sup>4,5,19</sup> However, as energy gaps decrease in the case of near infrared (NIR), with wavelengths in the range of 700 – 1,000 nm, and short-wave infrared (SWIR) dye molecules in the range of 1,000 – 2,000 nm, one may anticipate more direct role of NDCs between the excited and ground electronic states.

A recent work<sup>20</sup> by Friedman *et al.* reported fairly universal energy gap law<sup>21,22</sup> behavior of nonradiative decay rates for a broad class of NIR and SWIR dye

molecules. Similar observation was reported more recently for different kinds of NIR dye molecules based on single molecule spectroscopy as well.<sup>23</sup> The observed experimental trends<sup>20,23</sup> have significant implications because they suggest simple direct nonadiabatic transitions through NDC terms as major routes for nonradiative decays. However, as yet, detailed mechanisms involved in such universal energy gap law behavior have not been verified quantitatively at theoretical level. Given the growing importance of NIR and SWIR chromophores in biological imaging applications<sup>24–27</sup>, understanding how NDCs pose limitations on lifetimes of excited states is of particular interest. The present letter addresses this issue.

We here report comparative computational and experimental studies of two similar dye molecules, 7-dimethylamino flavylum pentamethine (Flav5) and 7-dimethylamino flavylum heptamethine (Flav7) and some deuterated forms of the latter synthesized recently (see SI for experimental details). Flav5 and Flav7 are NIR/SWIR dye molecules with similar structural motifs (see Fig. 1), but their nonradiative decay rates, 3.2 ns<sup>-1</sup> (Flav5) and 14.8 ns<sup>-1</sup> (Flav7), are different by about a factor of five.

For each molecule, we conducted optimization of the ground electronic state ( $S_0$ ) structure employing the density functional theory (DFT) method,<sup>28–30</sup> in the presence of a counter ion,  $\text{BF}_4^-$ , by employing the CAM-B3LYP functional<sup>31</sup> and the 6-311+G basis set. The calculated values for the vertical  $S_0 \rightarrow S_1$  transition are 2.2801 eV for Flav5 and 2.0599 eV for Flav7. Excitation energies calculated by other functionals are also provided in SI. Using the optimized ground state structure as the initial guess, we also optimized the structure of the excited state ( $S_1$ ) for each molecule using the time dependent DFT (TD-DFT) method.<sup>28,32,33</sup> The same basis of

<sup>a)</sup>Electronic mail: seogjoo.jang@qc.cuny.edu

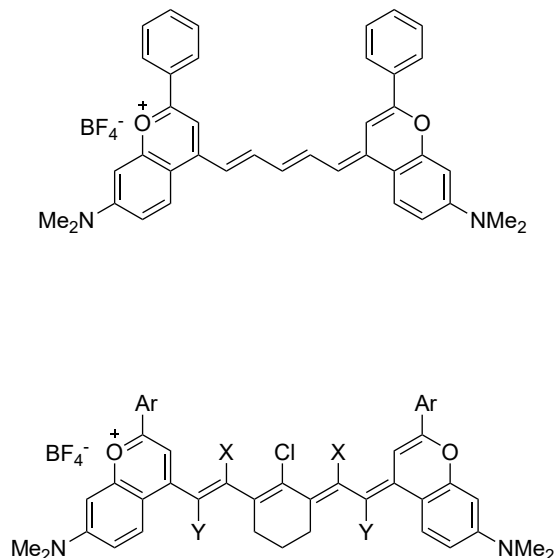


FIG. 1. Comparison of the two organic dye molecules Flav5 (upper panel) and Flav7 (lower panel). For the latter, X represent positions of hydrogen atoms being deuterated and Y represents those for which 30% of hydrogen atoms are deuterated. Flav7 with all hydrogen atoms in the aryl rings deuterated are also considered.

6-311+G and CAM-B3LYP functional were used. Calculated values of vertical  $S_1 \rightarrow S_0$  transition energies are 2.0935 eV for Flav5 and 1.8835 eV for Flav7. Calculated values of vertical emission energies based on other functionals are also provided in SI.

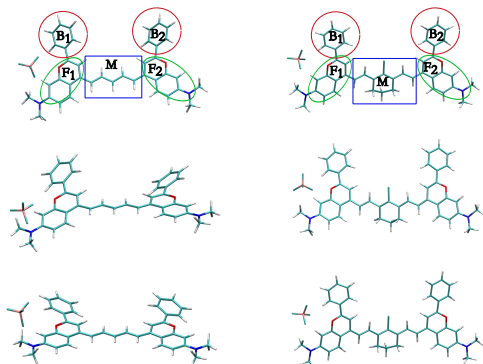


FIG. 2. Comparison of the structures of Flav5 (left column) and Flav7 (right column) dye molecules. The top row provides chemical structures indicating different sections with different labels. The middle row shows optimized structures for the  $S_0$  state, and the bottom row those for the  $S_1$  state.

In Fig. 2, the optimized structures for both dye molecules are shown. Structures shown at the top include labels for different parts of the molecule, which are used for providing a more detailed analyses below. For each molecule, the structure of  $S_0$  state is asymmetric, where the F1 flavylium heterocycle is tilted with respect

to the molecular plane, while the F2 heterocycle is nearly coplanar with the polymethine M section. The angle between the F1 heterocycle and the M section is  $18.0^\circ$  for Flav5 and  $26.0^\circ$  for Flav7. The B1 ring has an angle of  $20.4^\circ$  and  $25.0^\circ$  for Flav5 and Flav7 respectively, and the angle of the B2 phenyl group is about  $30.0^\circ$  w.r.t the molecular plane in both dyes, although they are in opposite directions. Thus, for the  $S_0$  state, the major structural difference of the two dye molecules lies in detailed orientational features of ring parts. On the other hand, for the  $S_1$  states, structures are similar and more symmetric, with B1 and B2 heterocycles at about  $17^\circ$  w.r.t the molecular plane. Both F1 and F2 parts are nearly coplanar with the M section, which is flat for Flav5 but is concave for Flav7 due to the presence of bridging  $sp^3$  carbons in the 7-methine M group.

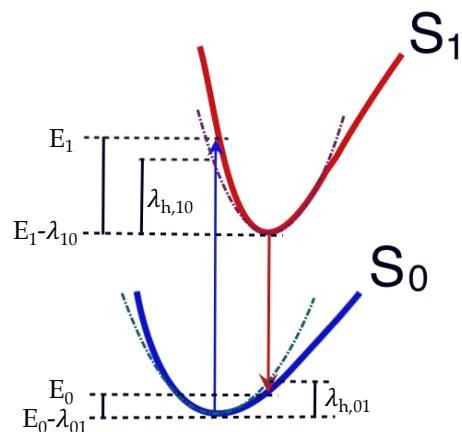


FIG. 3. A schematic of adiabatic potential energy surfaces for  $S_0$  (lower blue line) and  $S_1$  (upper red line) electronic states, which are in general anharmonic, and relevant energies.  $\lambda_{10}$  is the reorganization energy in the  $S_1$  state from the minimum energy structure of  $S_0$  to the optimized structure of  $S_1$ , and  $\lambda_{01}$  is the reorganization energy in the  $S_0$  state from the minimum energy structure of  $S_1$  to the optimized structure of  $S_0$ . Note that  $\tilde{E}_0 = E_0 - \lambda_{01}$  and  $\tilde{E}_1 = E_1 - \lambda_{10}$ . Reorganization energies within the harmonic approximation,  $\lambda_{h,10}$  and  $\lambda_{h,01}$  are also shown (see text for more detailed explanation).

For theoretical calculation of absorption and emission lineshapes, we evaluated Huang-Rhys (HR) factors<sup>34</sup> for both the vertical  $S_0 \rightarrow S_1$  transition at the optimized structure of  $S_0$  and also those for  $S_1 \rightarrow S_0$  transition at the optimized structure of  $S_1$ . For each molecule, there were clear differences between the two distributions of HR factors at  $S_0$  and  $S_1$  states, which reflects the presence of significant anharmonic effects. We account for such anharmonic contributions by introducing two different baths of harmonic oscillators defined differently depending on the structure of the initial state as de-

scribed below. Before providing more detailed description of models, we find it useful to clarify notations we adopt in this work.  $S_0$  and  $S_1$  denote the whole set of the ground and the first excited adiabatic electronic states, respectively, parametrized by nuclear coordinates. On the other hand, we introduce two diabatic states based on crude adiabatic approximation,  $|\tilde{S}_0\rangle$  and  $|\tilde{S}_1\rangle$ , determined at the minimum nuclear coordinates of the  $S_0$  surface, and another two diabatic states,  $|S_0\rangle$  and  $|\tilde{S}_1\rangle$ , determined at the minimum nuclear coordinates of the  $S_1$  surface.

Thus, we assume that the molecular Hamiltonian near the structure optimized for the  $S_0$  state of each molecule, can be approximated by the following model:

$$\hat{H}_0 = \tilde{E}_0 |\tilde{S}_0\rangle\langle\tilde{S}_0| + \left\{ E_1 + \sum_n \hbar\omega_n g_{n,10} (\hat{b}_n + \hat{b}_n^\dagger) \right\} |S_1\rangle\langle S_1| + \sum_n \hbar\omega_n (\hat{b}_n^\dagger \hat{b}_n + \frac{1}{2}),$$

where  $\tilde{E}_0$  and  $E_1$  are electronic energies of  $S_0$  and  $S_1$  states respectively for a fully optimized structure of the molecule in the  $S_0$  state, and  $\hat{b}_n$  and  $\hat{b}_n^\dagger$  represent lowering and raising operators for each harmonic oscillator normal mode of molecular vibrations calculated for the optimized structure of the  $S_0$  state (see Fig. 3 for a schematic illustration). The coupling constant  $g_{n,10}$  represents the extent of displacement of the  $n$ th normal mode upon excitation, the square of which is the corresponding HR factor for the  $S_0 \rightarrow S_1$  transition near the structure optimized for the  $S_0$  state. Note that the tilde symbol in  $\tilde{E}_0$  indicates that it is the energy for the fully relaxed (optimized) structure of the  $S_0$  state, in contrast to  $E_1$ .

Thus,  $E_1 - \tilde{E}_0$  is the vertical excitation energy for the  $S_0 \rightarrow S_1$  transition at the optimized structure of  $S_0$ .

On the other hand, for the structures optimized at the  $S_1$  state, we assume that the molecular Hamiltonian can be approximated by the following model:

$$\hat{H}_1 = \left( E_0 + \sum_n \hbar\omega_n g_{n,01} (\hat{b}_n + \hat{b}_n^\dagger) \right) |S_0\rangle\langle S_0| + \tilde{E}_1 |\tilde{S}_1\rangle\langle\tilde{S}_1| + \sum_n \hbar\omega_n (\hat{b}_n^\dagger \hat{b}_n + \frac{1}{2}),$$

where  $E_0$  and  $\tilde{E}_1$  are electronic energies of  $S_0$  and  $S_1$  states respectively for a fully optimized structure of the molecule in the  $S_1$  state, and  $\hat{b}_n$  and  $\hat{b}_n^\dagger$  represent lowering and raising operators for each harmonic oscillator normal mode of molecular vibrations calculated for the optimized structure of the  $S_1$  state (see Fig. 3 for a schematic illustration). The coupling constant  $g_{n,01}$  represents the extent of displacement of the  $n$ th normal mode, the square of which is the corresponding HR factor, for the  $S_1 \rightarrow S_0$  transition near the structure optimized for the  $S_1$  state.

Note that  $\tilde{E}_1 = E_1 - \lambda_{10}$  and  $E_0 = \tilde{E}_0 + \lambda_{01}$  (see Fig. 3). Thus,  $\lambda_{10}$  is the reorganization energy in the  $S_1$  electronic state for the structural change from that of the minimum  $S_0$  energy to that of  $S_1$ . On the other hand,  $\lambda_{01}$  is the reorganization energy in the  $S_0$  electronic state for the structural change from that of the minimum  $S_1$  energy to that of  $S_0$ . Thus,  $\tilde{E}_1 - E_0$  is the vertical emission energy for the transition to  $S_0$  from the fully relaxed  $S_1$  state. Note also that the harmonic oscillator bath modes in eqs. 1 and 2 are different but are denoted with the same labels. Experimental and theoretical values of  $E_1 - \tilde{E}_0$  and  $\tilde{E}_1 - E_0$  are compared in Table I. Theoretical values of reorganization energies for both the ground and excited state energies are provided as well.

TABLE I. Theoretical and experimental energy gaps for Flav 5 and Flav 7. Theoretical values of reorganization energies are also shown. Note that  $\lambda_{10} = E_1 - \tilde{E}_1$  and  $\lambda_{01} = E_0 - \tilde{E}_0$ .

Dye	$E_1 - \tilde{E}_0$ (eV)		$\tilde{E}_1 - E_0$ (eV)		$\lambda_{10}$ (eV)	$\lambda_{h,10}$ (eV)	$\lambda_{01}$ (eV)	$\lambda_{h,10}$ (eV)
	Exp.	Theory	Exp.	Theory				
Flav5	1.440	2.2801	1.378	2.0935	0.817	0.455	0.630	0.349
Flav7	1.207	2.0599	1.177	1.8835	0.701	0.631	0.524	0.283

Let us define the following bath spectral densities:

$$\mathcal{J}_{ij}(\omega) = \pi\hbar \sum_n \delta(\omega - \omega_n) \omega_n^2 g_{n,ij}^2. \quad (3)$$

where  $i, j = 1, 0$  (for eq. 1) or  $0, 1$  (for eq. 2), and the corresponding real and imaginary parts of the lineshape

function:

$$\begin{aligned} G_{R,ij}(t) &= \frac{1}{\pi\hbar} \int_0^\infty d\omega \frac{\mathcal{J}_{ij}(\omega)}{\omega^2} \coth\left(\frac{\hbar\omega}{2k_B T}\right) (1 - \cos(\omega t)) \mathcal{A} \\ G_{I,ij}(t) &= \frac{1}{\pi\hbar} \int_0^\infty d\omega \frac{\mathcal{J}_{ij}(\omega)}{\omega^2} (\sin(\omega t) - \omega t) \\ &= \frac{1}{\pi\hbar} \int_0^\infty d\omega \frac{\mathcal{J}_{ij}(\omega)}{\omega^2} \sin(\omega t) - \frac{\lambda_{h,ij}}{\hbar} t, \end{aligned} \quad (5)$$

with  $\lambda_{h,ij} = \hbar \sum_n \omega_n g_{n,ij}^2$ . Note that  $\lambda_{h,10}$  and  $\lambda_{h,01}$  are harmonic approximations for  $\lambda_{10} = E_1 - \tilde{E}_1$  and  $\lambda_{01} = E_0 - \tilde{E}_0$ , as indicated in Fig. 3. Thus,  $\lambda_{10} - \lambda_{h,10}$  represents contributions of anharmonicity in the  $S_1$  surface, whereas  $\lambda_{01} - \lambda_{h,01}$  represents that in the  $S_0$  surface. In the simplest displaced harmonic oscillator model for which  $S_1$  and  $S_0$  are parabolic forms of the same curvature,  $\lambda_{01} = \lambda_{10} = \lambda_{h,01} = \lambda_{h,10}$ .

The normalized absorption lineshape for  $S_0 \rightarrow S_1$  transition, for the Hamiltonian of eq. 1, based on the Fermi's golden rule (FGR) for interaction with radiation within the dipole approximation,<sup>35</sup> can be expressed as

$$I_{S_0 \rightarrow S_1}(\omega) = \frac{1}{2\pi} \int_{-\infty}^{\infty} dt \exp \left\{ i \left( \omega - \frac{(E_1 - \tilde{E}_0)}{\hbar} \right) t - G_{R,10}(t) - iG_{I,10}(t) \right\}. \quad (6)$$

On the other hand, the normalized emission lineshape for  $S_1 \rightarrow S_0$  transition, for the Hamiltonian of eq. 2, can be expressed as<sup>35</sup>

$$I_{S_1 \rightarrow S_0}(\omega) = \frac{1}{2\pi} \int_{-\infty}^{\infty} dt \exp \left\{ i \left( \omega - \frac{(\tilde{E}_1 - E_0)}{\hbar} \right) t - G_{R,01}(t) + iG_{I,01}(t) \right\}. \quad (7)$$

For actual calculation of lineshapes, we employed a Lorentzian function for the delta function in eq. 3. Thus, the following approximations were used.

$$\begin{aligned} \mathcal{J}_{ij}(\omega) &\approx \hbar \sum_n \frac{\omega_n^2 g_{n,ij}^2 \sigma}{\sigma^2 + (\omega - \omega_n)^2} \\ &= 2\pi c \hbar \sum_n \frac{\tilde{\nu}_n^2 g_{n,ij}^2 \tilde{\nu}_\sigma}{\tilde{\nu}_\sigma^2 + (\tilde{\nu}_n - \tilde{\nu})^2}, \end{aligned} \quad (8)$$

where  $\tilde{\nu} = \omega/(2\pi c)$ ,  $\tilde{\nu}_n = \omega_n/(2\pi c)$ , and  $\tilde{\nu}_\sigma = \sigma/(2\pi c)$ . The choice of  $\tilde{\nu}_\sigma$  can be made such that it is small enough to discern all different vibrational frequencies, and we found that the choice of  $\tilde{\nu}_\sigma = 22 \text{ cm}^{-1}$  reasonable. The resulting spectral densities are provided in SI.

Figure 4 compares calculated absorption and emission lineshapes for Flav5 and Flav7 respectively with experimental lineshapes. The peak maxima of theoretical lineshapes were shifted uniformly to match experimental ones as indicated in the figure caption, but no other corrections were made. Considering the simplicity of underlying models and the fact that solvation effects have not been included, the agreements are excellent. This suggests that major vibronic interactions are reasonably represented by normal modes of molecular vibrations, modeled as harmonic oscillators, and that contributions of solvents are rather minor. It is worth noting that small peaks around 500 nm in experimental absorption lineshapes correspond to excitations to higher electronic

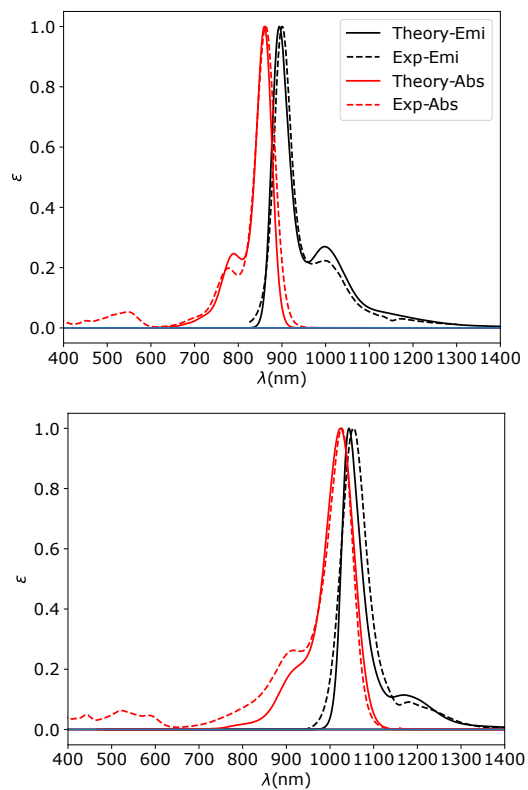


FIG. 4. Absorption ( $S_0 \rightarrow S_1$ ) and emission ( $S_1 \rightarrow S_0$ ) lineshapes for Flav5 (upper) and Flav7 (lower). Experimental lineshapes in solution phase are compared with theoretical lineshapes of isolated molecules, which were shifted to match the corresponding maxima of experimental spectra. For the absorption, the shifts were 1.423 eV for Flav5 and 1.191 eV for Flav7. For the emission, the shifts were 1.405 eV for Flav5 and 1.185 eV for Flav7. We also normalized heights with respect to those of their maxima.

states, which are not included in our calculations. In addition, while other small disagreements between theoretical and experimental lineshapes could in principle be accounted for by inclusion of solvent effects, simple calculations based on polarizable continuum model turned out to worsen theoretical lineshapes compared to experimental ones (see SI). Therefore, more accurate solvation model is necessary for better quantitative agreement.

As can be seen from Fig. 4, the absorption lineshape for each molecule has a prominent sideband followed by broad tail in the blue region. For Flav5, the major sideband is attributed to two groups of normal modes (see SI for the depiction of major normal modes.). The first group corresponds to wagging motions of H atoms at  $1,026 \text{ cm}^{-1}$ , which are broadened by those of heavy atoms at around  $675 \text{ cm}^{-1}$ . The second group consists of the scissoring motion of heavy atoms at  $1,237 \text{ cm}^{-1}$  and H atoms at  $1,242 \text{ cm}^{-1}$  respectively. The broad tail region is due to the high energy modes and are related to the rocking motion of H atoms in the structure and the stretching motion of H atoms in the aliphatic chain. For

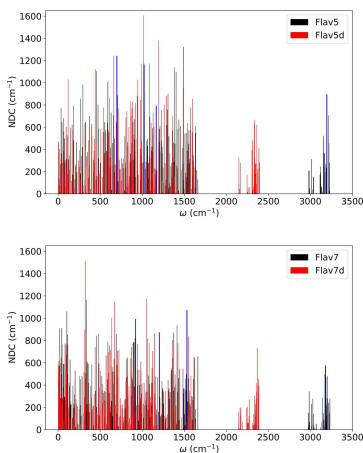


FIG. 5. Nonadiabatic couplings projected on to each normal mode for the Flav5 (upper panel) and Flav7 (lower panel). Black lines represent results for original molecules and red lines represent those for fully deuterated ones.

Flav7, the major sideband is due to the wagging motion of the benzene ring carbons at  $825 \text{ cm}^{-1}$ , scissoring motion of H atoms at  $1,252 \text{ cm}^{-1}$ , and the wagging motion of H atoms at  $1,509 \text{ cm}^{-1}$ . The broad blue tail is also contributed by these wagging modes, with the addition of the stretching motion of H atoms within the central parts of molecules. The stretching of the aliphatic chain at  $2,980 \text{ cm}^{-1}$  and the stretching of H atoms in aromatic rings at  $3,150 \text{ cm}^{-1}$  also make some contributions. Similar features appear in the respective emission lineshapes on the red side of major peaks. Detailed data of the bath spectral densities for all the transitions are provided in SI.

For the optimized structure in the  $S_1$  state of each molecule, we calculated first NDC terms<sup>8,9</sup> in cartesian coordinates, which were then projected onto different mass weighted normal modes of vibration. The resulting expression is as follows:

$$\text{NDC}_j = \frac{|\langle \tilde{S}_1 | \left( \partial \hat{H}_e(\mathbf{q}) / \partial q_{1,j} \right) |_{\mathbf{q}_1=0} | S_0 \rangle|}{\tilde{E}_1 - E_0} \quad (9)$$

where  $q_{1,j}$  represents the  $j$ th mass-weighted normal mode in the  $S_1$  state around its minimum energy structure. Detailed derivation of the above expression starting from full molecular Hamiltonian in the adiabatic basis<sup>4,5</sup> is provided in SI. We also calculated the NDC terms for partially and fully deuterated Flav5 and Flav7 molecules. Figure 5 shows distributions of these projected NDC terms for original and fully deuterated molecules. Results in Fig. 5 show broad distributions of NDC terms up to about  $1,600 \text{ cm}^{-1}$  and another well separated high frequency bands, which correspond to C-H (or C-D) stretching modes. It is interesting to note that the contributions of these high frequency modes are rather small compared to those due to broad low frequency modes. To examine the validity of our simple displaced harmonic oscil-

ator models, we also calculated the Duschinsky rotation matrix<sup>11,12</sup> from the displacements of the nuclei in the normal modes. Results provided in SI suggest that Duschinsky effects are not likely to affect the major conclusion of this work.

We calculated nonradiative decay rates for  $S_1 \rightarrow S_0$  transitions also using FGR within the Condon approximation, assuming an effective constant coupling determined as an average of the first derivative coupling terms. In more detail, we averaged projections of NDC terms on different normal modes as follows:

$$J_{eff} = \hbar \sum_{j=1}^{N_v} \left( \frac{\sum_{v_j=0}^{\infty} \langle p_{v_j}^2 \rangle^{1/2} e^{-\hbar\omega_j(v_j+1/2)/(k_B T)}}{\sum_{v_j=0}^{\infty} e^{-\hbar\omega_j(v_j+1/2)/(k_B T)}} \right) \text{NDC}_j, \quad (10)$$

where  $\langle p_{v_j}^2 \rangle^{1/2} = \sqrt{\hbar\omega_j(v_j + \frac{1}{2})}$ , the root-mean-square momentum of each vibrational mode with vibrational quantum number  $v_j$ , and  $\text{NDC}_j$  is given by Eq. (9). Detailed derivation of the above expression and method of calculation are provided in SI. The resulting values of  $J_{eff}$  are provided in Table II.

For the calculation of non-radiative transition from the  $S_1$  state to the  $S_0$  state due to the effective electronic coupling  $J_{eff}$  given by eq. 10, we assume an effective two state model coupled to harmonic oscillator baths as follows:

$$\hat{H}_{nr} = \tilde{E}_1 |\tilde{S}_1\rangle \langle \tilde{S}_1| + \left( E_0 + \sum_n \hbar\omega_n g_{n,01} (\hat{b}_n + \hat{b}_n^\dagger) \right) |S_0\rangle \langle S_0| + J_{eff} (|\tilde{S}_1\rangle \langle S_0| + |S_0\rangle \langle \tilde{S}_1|) + \sum_n \hbar\omega_n \left( \hat{b}_n^\dagger \hat{b}_n + \frac{1}{2} \right). \quad (11)$$

Note that the above model Hamiltonian is the same as that used for the emission lineshape except that the two electronic states are now coupled by  $J_{eff}$ .

The FGR rate for the above model Hamiltonian is as follows:<sup>35</sup>

$$k_{FG} = \frac{J_{eff}^2}{\hbar^2} \int_{-\infty}^{\infty} dt \exp \left\{ \frac{i}{\hbar} (\tilde{E}_1 - E_0)t - G_{R,01}(t) - G_{I,01}(t) \right\}, \quad (12)$$

where  $G_{R,01}(t)$  and  $G_{I,01}(t)$  are respectively defined by eqs. 4 and 5 with  $i = 0$  and  $j = 1$ .

Figure 6 shows calculated nonradiative rates for a range of energy gap values. The actual values of energy gaps, which are shown as vertical lines, are  $1.378 \text{ eV}$  for Flav5 and  $1.177 \text{ eV}$  for Flav7. These confirm that actual transitions indeed occur within ranges where the energy gap law behavior<sup>21,22</sup> is expected to be observed. In order to determine the contribution of the high frequency C-H or C-D stretching modes to these rates, we also calculated rates with contributions of those modes to HR factors turned off. The resulting data are shown as red lines. Eliminating these high frequency contributions indeed reduce the rates, more significantly as the gap increases.

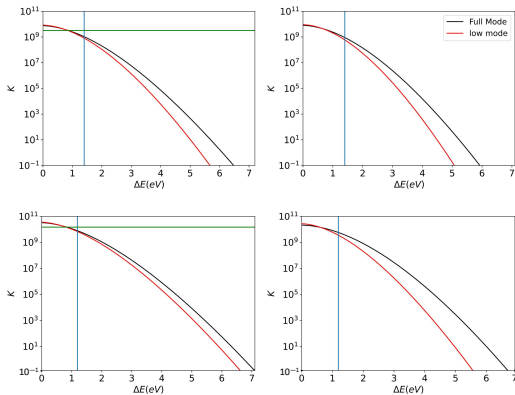


FIG. 6. Nonadiabatic transition rates (in logarithmic scale) versus energy gap for the  $S_1 \rightarrow S_0$  electronic transitions for both Flav5 (upper panel) and Flav7 (lower panel) dyes, where the vertical lines represent the experimental energy gap value between the two states,  $\tilde{E}_1 - E_0$ , which are 1.378 eV for Flav5 and 1.177 eV for Flav7. Rates versus the energy gap are shown for the original molecules (left) and deuterated (right) molecules. The experimental rates for the original molecules are shown as horizontal lines. Red curves represent transition rates calculated with the high energy vibrational modes nullified.

Table II shows values of theoretical rates determined at the positions of actual energy gap values in Fig. 6. Experimental nonradiative rates are also shown for comparison. The theoretical values are smaller than experimental ones, which suggest contributions of Duschinsky rotation effects<sup>10,40,41,43,44</sup> and non-Condon effects can be significant. Nonetheless, the theoretical trends agree well with experimental one. For both original and fully deuterated molecules, we also determined rates for the hypothetical situation where high frequency C-H or (C-D) stretching modes do not contribute. The resulting values are shown in parentheses. It is shown that contributions of high frequency modes to the total NDCs and rates are relatively small for these cases.

In addition to fully deuterated cases, we also calculated rates with partial deuteration. The Flav7 molecule denoted with m.D2 and m.D2.12 are those where the deuteration takes place at the aliphatic hydrogen whereas that with Ar.D10 has aromatic hydrogens deuterated. These changes result in modest reduction of effective couplings and rates. This indicates that the tunneling of hydrogen-involving vibrational modes indeed make some contributions to the rates but are not a determining factor. We also find that our computational results are consistent with experimental data.

In order to examine the possibility of alternative nonradiative decay processes through triplet states, we also determined first ( $T_1$ ) and second ( $T_2$ ) excited triplet states, and calculated FGR rates for the following four possible transitions:  $T_1 \rightarrow S_0$ ;  $T_2 \rightarrow S_0$ ;  $S_1 \rightarrow T_1$ ;  $S_1 \rightarrow T_2$ . The spectral densities of normal modes determined for the

TABLE II. Theoretical data for the effective electronic coupling  $J_{eff}$ , eq. 10, and the nonradiative FGR rate, eq. 12, for  $S_1 \rightarrow S_0$  transitions for Flav5, Flav5<sub>D</sub> (fully deuterated), Flav7, and Flav7<sub>D</sub> (fully deuterated), and partially deuterated Flav7 (with different subscripts representing parts of deuteration). Experimental nonradiative decay rates are also shown. For the calculation of theoretical rates, experimental values of the energy gap, as listed in Table I were used. Theoretical data for the hypothetical cases where the high frequency C – H (or C – D) stretching modes are turned off are also shown in parentheses.

Dye	Theory ( $S_1 \rightarrow S_0$ )		$k_{exp}(\text{ns}^{-1})$
	$J_{eff}(\text{cm}^{-1})$	$k_{nr}(\text{ns}^{-1})$	
Flav5	425.3 (424.8)	1.041 (0.812)	3.2
Flav5 <sub>D</sub>	388.2 (388.1)	0.904 (0.600)	
Flav7	918.8 (917.4)	8.350 (7.297)	14.7
Flav7 <sub>D</sub>	756.8 (756.5)	6.081 (5.660)	
Flav7 <sub>mD2</sub>	596.0	5.133	14.1
Flav7 <sub>mD2.12</sub>	654.8	3.727	13.8
Flav7 <sub>ArD10</sub>	482.3	1.984	13.5

$S_1$  were used and the spin-orbit coupling constants, determined as detailed in SI, were used for the effective electronic coupling in eq. 12. Calculated values provided in Table S1 of SI show that all of the singlet-triplet transition rates are less than  $10^5 \text{ s}^{-1}$ . Although approximations were involved in these calculations, it is not likely that more accurate calculations would significantly alter the order of estimates. Thus, we believe these results serve as strong evidence that transitions through triplet states do not have appreciable contributions for these dye molecules. Regarding the possibility of going through conical intersections followed by activated processes, it is not plausible either because activated crossing in the excited state manifold, which would be the rate determining step, should be insensitive to the energy gap between excited and ground electronic states.

In summary, we have conducted computational modeling and theoretical analyses of non-radiative decay rates from the first singlet excited states for two NIR/SWIR dye molecules, Flav5 and Flav7, which were shown to exhibit the energy gap law behavior. The trends of our theoretical rates are in good agreement with those of experimental data. Additional calculations for deuterated dye molecules corroborate our conclusion, and indeed serve as a good evidence that the cumulation of all NDC terms along all Franck-Condon modes in the excited electronic state provide the major route for the nonradiative decay of NIR/SWIR dye molecules exhibiting the energy gap law behavior. Pending future efforts for broader class of dye molecules and validation through higher level the-

oretical/computational studies<sup>10,40,41,43,44</sup> that also include Duschinsky, non-Condon effects, or anharmonic contributions, the present work also provides simple theoretical models to semiquantitatively describe the energy gap law behavior of nonradiative decays of NIR/SWIR dye molecules.

## ACKNOWLEDGMENTS

SJJ acknowledges partial support from the National Science Foundation (CHE-1900170) during the initial stage of this project, and major support from the US Department of Energy, Office of Sciences, Office of Basic Energy Sciences (DE-SC0021413). SJJ also acknowledges support from Korea Institute for Advanced Study through its KIAS Scholar program. JRC, HCF, CG and EMS are supported by NSF Grant CHE-2204263. JRC would also like to acknowledge the Cottrell foundation for support.

- <sup>1</sup>Born, M.; Oppenheimer, J. R. Zur quantentheorie der molekeln. *Ann. Phys. (Berl.)* **1927**, *389*, 457–484.
- <sup>4</sup>Jang, S. J. *Quantum Mechanics for Chemistry*; Springer Nature: New York, 2023.
- <sup>3</sup>Baer, M. Introduction to the theory of electronic non-adiabatic coupling terms in molecular systems. *Phys. Rep.* **2002**, *358*, 75–142.
- <sup>4</sup>Yonehara, T.; Hanasaki, K.; Takatsuka, K. Fundamental approaches to nonadiabaticity: Toward a chemical theory beyond the Born Oppenheimer paradigm. *Chem. Rev.* **2012**, *112*, 499–542.
- <sup>5</sup>Jasper, A. W.; Zhu, C.; Nangia, S.; Truhlar, D. G. Introductory lecture: Nonadiabatic effects in chemical dynamics. *Faraday Discuss.* **2004**, *127*, 1.
- <sup>6</sup>Chen, X.-K.; Ravva, M. K.; Li, H.; Ryno, S. M.; Brédas, J.-L. Effect of Molecular Packing and Charge Delocalization on the Nonradiative Recombination of Charge-Transfer States in Organic Solar Cells. *Adv. Ener. Mater.* **2016**, *6*, 1601325.
- <sup>7</sup>Uratani, H.; Morioka, T.; Yoshikawa, T.; Nakai, H. Fast Nonadiabatic Molecular Dynamics via Spin-Flip Time-Dependent Density-Functional Tight-Binding Approach: Application to Nonradiative Relaxation of Tetraphenylethylene with Locked Aromatic Rings. *J. Chem. Theory Comput.* **2020**, *16*, 7299–7313.
- <sup>8</sup>Tully, J. C. Perspective: Nonadiabatic dynamics theory. *J. Chem. Phys.* **2012**, *137*, 22A301.
- <sup>9</sup>Song, H.; Fischer, S. A.; Zhang, Y.; Cramer, C. J.; Mukamel, S.; Govind, N.; Tretiak, S. First principles nonadiabatic excited-state molecular dynamics in NWChem. *J. Chem. Theory Comput.* **2020**, *16*, 6418–6427.
- <sup>10</sup>Zhao, L.; Tao, Z.; Pavosevic, F.; Wildman, A.; Hammes-Schiffer, S.; Li, X. Real-time time-dependent nuclear-electronic orbital approach: Dynamics beyond the Born-Oppenheimer approximation. *J. Phys. Chem. Lett.* **2020**, *11*, 4052–4058.
- <sup>11</sup>Curchod, B. F. E.; Rauer, C.; Marquetand, P.; González, L.; Martínez, T. GAIMS—Generalized Ab Initio Multiple Spawning for both internal conversion and intersystem crossing processes. *J. Chem. Phys.* **2016**, *144*, 101102.
- <sup>12</sup>Bian, X.; Wu, Y.; Teh, H.-H.; Zhou, Z.; Chen, H.-T.; Subotnik, J. E. Modeling nonadiabatic dynamics with degenerate electronic states, intersystem crossing, and spin separation: A key goal for chemical physics. *J. Chem. Phys.* **2021**, *154*, 110901.
- <sup>13</sup>Prezhdo, O. V. Modeling non-adiabatic dynamics in nanoscale and condensed matter systems. *Acc. Chem. Res.* **2021**, *54*, 4329–4249.
- <sup>14</sup>Shu, Y.; Zhang, L.; Chen, X.; Sun, S.; Huang, Y.; Truhlar, D. G. Nonadiabatic dynamics algorithms with only potential energies and gradients: Curvature-driven coherent switching with decay of mixing and curvature-driven trajectory surface hopping. *J. Chem. Theory Comput.* **2022**, *18*, 1320–1328.
- <sup>15</sup>Ishikawa, H.; Noyes, A. W. Photosensitization by benzene vapor: Biacetyl. The triplet state of benzene. *J. Chem. Phys.* **1962**, *37*, 583–591.
- <sup>16</sup>Laposa, J. D.; Lim, E. C.; Kellogg, R. E. Radiationless transitions and deuterium effect on fluorescence lifetimes of some aromatic hydrocarbons. *J. Chem. Phys.* **1965**, *42*, 3025–3026.
- <sup>17</sup>Kathayat, R. S.; Yang, L.; Sattasathuchana, T.; Zoppi, L.; Baldrige, K. K.; Linden, A.; Finney, N. S. On the origins of nonradiative excited state relaxation in aryl sulfoxides relevant to fluorescent chemosensing. *J. Am. Chem. Soc.* **2016**, *138*, 15889–15895.
- <sup>18</sup>Hare, P. M.; Crespo-Hernández, C. E.; Kohler, B. Internal conversion to the electronic ground state occurs via two distinct pathways for pyrimidine bases in aqueous solution. *Proc. Natl. Acad. Sci., USA* **2007**, *104*, 435–440.
- <sup>19</sup>A. F. Izmaylov, D. Mendive-Tapia, M. J. Bearpark, M. A. Robb, J. C. Tully, and M. J. Frisch, Nonequilibrium Fermi golden rule for electronic transitions through conical intersection. *J. Chem. Phys.* **2011**, *135*, 234106.
- <sup>20</sup>Friedman, H. C.; Cosco, E. D.; Atallah, T. L.; Jia, S.; Sletten, E. M.; Caram, J. R. Establishing design principles for emissive organic SWIR chromophores from energy gap laws. *Chem* **2021**, *7*, 1–18.
- <sup>21</sup>Englman, R.; Jortner, J. The energy gap law for radiationless transitions in large molecules. *Mol. Phys.* **1970**, *18*, 145–164.
- <sup>22</sup>Jang, S. J. A simple generalization of the energy gap law for nonradiative processes. *J. Chem. Phys.* **2021**, *155*, 164106.
- <sup>23</sup>Erker, C.; Basche, T. The energy gap law at work: Emission yield and rate fluctuations of single NIR emitters. *J. Am. Chem. Soc.* **2022**, *144*, 14053–14056.
- <sup>24</sup>Thimsen, E.; Sadtler, B.; Berezin, M. Y. Shortwave-infrared (SWIR) emitters for biological imaging: a review of challenges and opportunities. *Nanophotonics* **2017**, *6*, 1043–1054.
- <sup>25</sup>Xie, Y.; Liu, W.; Deng, W.; Wu, H.; Wang, W.; Si, Y.; Zhan, X.; Gao, C.; Chen, X.-K.; Wu, H. et al. Bright short-wavelength infrared organic light-emitting devices. *Nat. Photon* **2022**, *16*, 752–761.
- <sup>26</sup>Pascal, S.; David, S.; Andraud, C.; Maury, O. Near-infrared dyes for two-photon absorption in the short-wavelength infrared: strategies towards optical power limiting. *Chem. Soc. Rev.* **2021**, *50*, 6613–6658.
- <sup>27</sup>Li, C.; Chen, G.; Zhang, Y.; Wu, F.; Wang, Q. Advanced Fluorescence Imaging Technology in the Near-Infrared-II Window for Biomedical Applications. *J. Am. Chem. Soc.* **2020**, *142*, 14789–14804.
- <sup>28</sup>Parr, R. G.; Yang, W. *Density-Functional Theory of Atoms and Molecules*; Oxford University Press: Oxford, 1989.
- <sup>29</sup>Dreizler, R. M.; Gross, E. K. U. *Density Functional Theory — An Approach to the Quantum Many-Body Problem*; Springer: Berlin, 1990.
- <sup>30</sup>Engel, E.; Dreizler, R. M. *Density Functional Theory: An advanced course*; Springer, 2011.
- <sup>31</sup>Yanai, T.; Tew, D. P.; Handy, N. C. A new hybrid exchange–correlation functional using the Coulomb-attenuating method (CAM-B3LYP). *Chem. Phys. Lett.* **2004**, *393*, 51–57.
- <sup>32</sup>Gross, E. K. U.; Ullrich, C. A.; Gossmann, U. J. In *Density Functional Theory*; Gross, E. K. U., Ed.; Plenum Press: New York, 1995; pp 149–171.
- <sup>33</sup>Marques, M. A. L.; Gross, E. K. U. In *A Primer in Density Functional Theory*; Fiolhais, C., Nogueira, F., Marques, M., Eds.; Springer: Berlin, 2003; pp 144–184.
- <sup>34</sup>Reimers, J. R. A practical method for the use of curvilinear coordinates in calculations of normal-mode-projected displacements and Duschinsky rotation matrices for large molecules. *J. Chem. Phys.* **2001**, *115*, 9103–9109.

- <sup>35</sup>Jang, S. J. *Dynamics of Molecular Excitons (Nanophotonics Series)*; Elsevier: Amsterdam, 2020.
- <sup>8</sup>Fatehi, S.; Alguire, E.; Shao, Y.; Subotnik, J. E. Analytic derivative couplings between configuration-interaction-singles states with built-in electron-translation factors for translational invariance. *J. Chem. Phys.* **2011**, *135*, 234105.
- <sup>9</sup>Ou, Q.; Bellchambers, G. D.; Furche, F.; Subotnik, J. E. First-order derivative couplings between excited states from adiabatic TDDFT response theory. *J. Chem. Phys.* **2015**, *142*, 064114.
- <sup>11</sup>Chang, J.-L. A new method to calculate Franck–Condon factors of multidimensional harmonic oscillators including the Duschinsky effect. *J. Chem. Phys.* **2008**, *128*, 174111.
- <sup>12</sup>Ruhoff, P. T.; Ratner, M. A. Algorithms for computing Franck–Condon overlap integrals. *Int. J. Quantum Chem.* **2000**, *77*, 383–392.
- <sup>40</sup>Mebel, A. M.; Hayashi, M.; Liang, K. K.; Lin, S. H. Ab Initio calculations of vibronic spectra and dynamics for small polyatomic molecules: Role of Duschinsky effect. *J. Phys. Chem. A* **1999**, *103*, 10674–10690.
- <sup>41</sup>Niu, Y.; Peng, Q.; Shuai, Z. Promoting-mode free formalism for excited state radiationless decay process with Duschinsky rotation effect. *Sci. China Ser. B-Chem.* **2008**, *51*, 1153–1158.
- <sup>10</sup>Niu, Y.; Peng, Q.; Deng, C.; Gao, X.; Shuai, Z. Theory of excited state decays and optical spectra: Application to polyatomic molecules. *J. Phys. Chem. A* **2010**, *114*, 7817–7831.
- <sup>43</sup>Borrelli, R.; Peluso, A. Perturbative calculation of Franck–Condon integrals: New hints for a rational implementation. *J. Chem. Phys.* **2008**, *129*, 064116.
- <sup>44</sup>Wang, Y.; Ren, J.; Shuai, Z. Evaluating the anharmonicity contributions to the molecular excited internal conversion rates with finite temperature TD-DMRG. *J. Chem. Phys.* **2021**, *154*, 214109.

## I. SUPPORTING INFORMATION

### A. Additional details and results of computation

All geometry optimizations were carried out employing the Gaussian 16 program package<sup>1</sup>, while calculation of electronic excitation energies, Huang-Rhys (HR) factors, spin-orbit couplings and non-adiabatic couplings were calculated employing the QCHEM program package.<sup>2</sup> Table III provide additional calculation results for the vertical absorption and emission energies based on different functionals.

TABLE III. Classical and quantum reorganization energies data for  $S_1 \rightarrow S_0$  transitions for Flav5 (F5), deuterated Flav5 (F5<sub>D</sub>), Flav7 (F7), and deuterated Flav7 (F7<sub>D</sub>).

System	XC-Functional	vertical abs (eV)	vertical emi (eV)
Flav5	CAM-B3LYP	2.2801	2.0935
	CAM-B3LYP ( $\omega = 250a.u.$ )	2.2498	2.0425
	B3LYP	2.1038	1.5808
	M06-L	1.7717	1.3145
Flav7	2.0599	1.8835	1.3593
	CAM-B3LYP ( $\omega = 250a.u.$ )	2.0349	1.8680
	B3LYP	1.9822	1.4708
	M06-L	1.6696	1.2022

Figures 7 and 8 show the bath spectral densities calculated according to Eq. (11) of the main text. Results for both original isolated molecules and fully deuterated molecules are shown. The corresponding absorption and emission lineshapes for fully deuterated molecules are shown in Fig. 9. The lineshapes for original molecules without deuteration, which were provided in Fig. 4 of the main text, are also shown for comparison. Note that normalizations of lineshapes in Fig. 9 are different from those in Fig. 4 of the main text.

In addition to the calculation of gas phase molecules, we also conducted calculations of molecules in dichloromethane (DCM) solvent, modeled at the level of polarizable continuum model (PCM)<sup>3</sup> with the value of the dielectric constant corresponding to that of DCM at room temperature,  $\epsilon = 8.93$ . The resulting lineshapes and bath spectral densities are shown in Figs. 10 and 11. While inclusion of solvent brings the excitation energy closer to experimental ones, the resulting lineshapes become even worse than isolated ones when compared with experimental data. We attribute this to that the continuum solvation model restricts the vibrational motion of molecules and makes HR factors become smaller than what they are in actual atomistic solvent environments.

### B. Normal Modes

Major normal modes contributing to the lineshapes for Flav5 and Flav7 are depicted in Figs. 12 and 13.



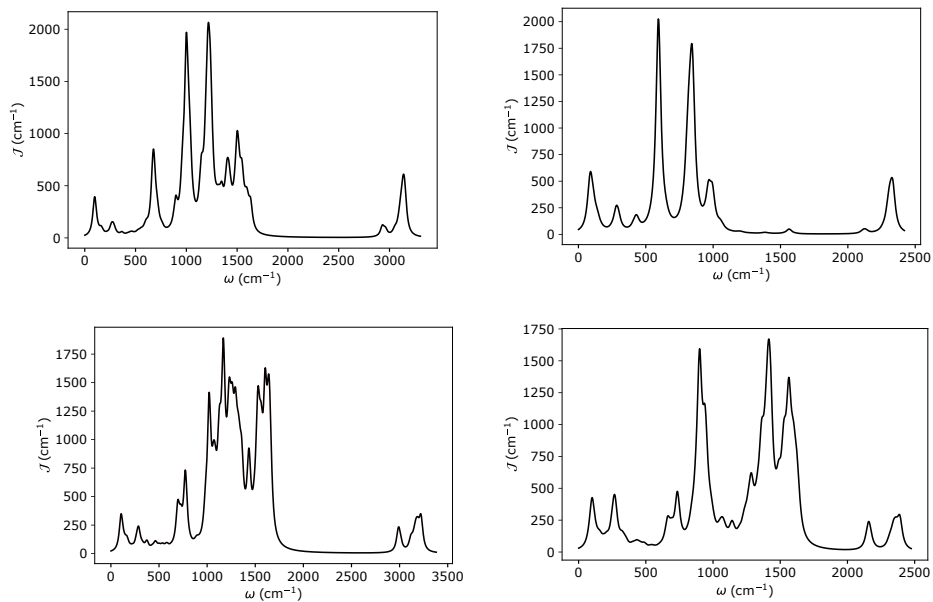


FIG. 7. Spectral density  $\mathcal{J}_{10}(\omega)$  (upper panels) and  $\mathcal{J}_{01}(\omega)$  (lower panels) for Flav5 for the isolated (left) and deuterated (right) molecules.

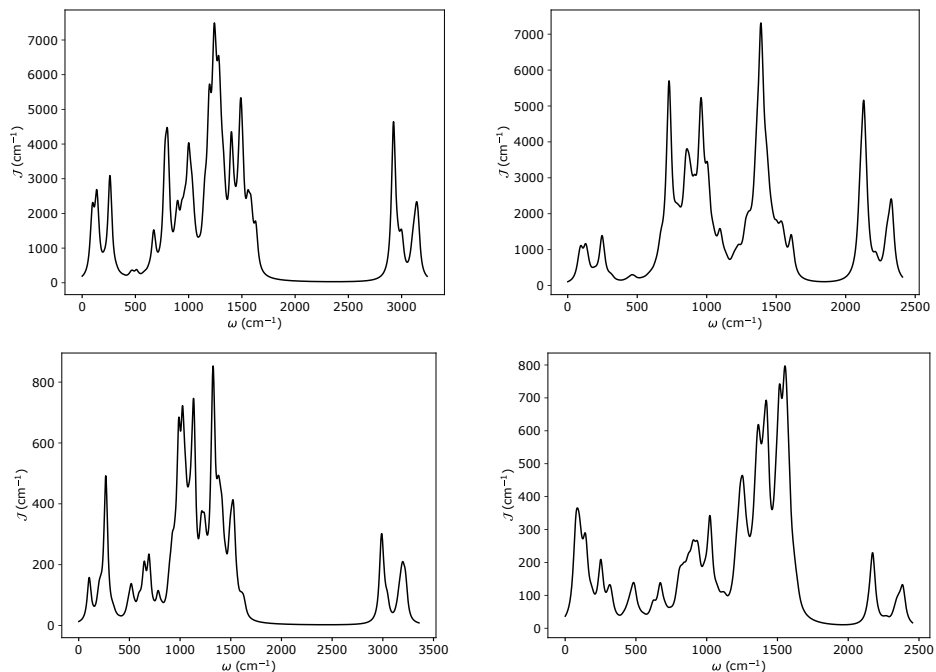


FIG. 8. Spectral density  $\mathcal{J}_{10}(\omega)$  (upper panels) and  $\mathcal{J}_{01}(\omega)$  (lower panels) for flav7 for the isolated (left) deuterated (right) molecules.

### C. Derivative nonadiabatic coupling between $S_1$ and $S_0$

We here provide a derivation and justification of the effective non-adiabatic coupling, Eq. (12) in the main text. Consider a molecule consisting of  $N_e$  electrons and  $N_u$  nuclei. The corresponding Hamiltonian (in atomic units) can be expressed as<sup>4</sup>

$$\hat{H} = \hat{H}_{en} + \hat{H}_{nu}, \quad (13)$$

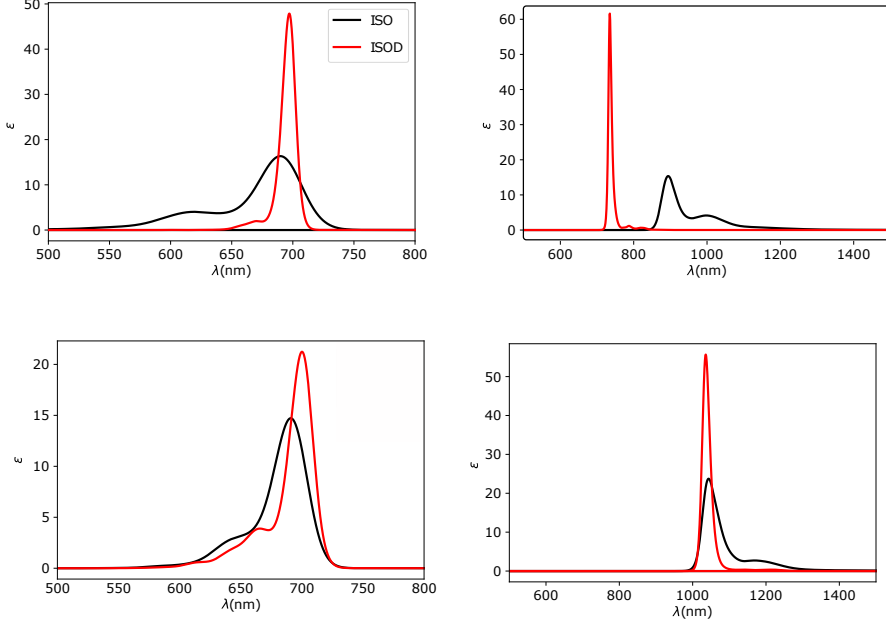


FIG. 9. Comparison of the absorption and emission spectra line shape for both isolated and deuterated conditions for the two chromophores Flav5 (upper panels) and Flav7 (lower panels) .

where

$$\hat{H}_{en} = \sum_{\mu=1}^{N_e} \frac{\hat{\mathbf{p}}_{\mu}^2}{2} - \sum_{\mu=1}^{N_e} \sum_{c=1}^{N_u} \frac{Z_c e^2}{|\hat{\mathbf{r}}_{\mu} - \hat{\mathbf{R}}_c|^2} + \frac{1}{2} \sum_{\mu=1}^{N_e} \sum_{\nu \neq \mu} \frac{1}{|\hat{\mathbf{r}}_{\mu} - \hat{\mathbf{r}}_{\nu}|}, \quad (14)$$

$$\hat{H}_{nn} = \sum_{c=1}^{N_u} \frac{\hat{\mathbf{P}}_c}{2M_c} + \frac{1}{2} \sum_{c=1}^{N_u} \sum_{c' \neq c} \frac{Z_c Z_{c'}}{|\hat{\mathbf{R}}_c - \hat{\mathbf{R}}_{c'}|}. \quad (15)$$

Let us consider the adiabatic electronic Hamiltonian  $\hat{H}_{en}(\mathbf{R})$ , which is the same as Eq. (14) except that all the nuclear position operator vector  $\hat{\mathbf{R}} \equiv (\hat{\mathbf{R}}_1, \dots, \hat{\mathbf{R}}_{N_u})^T$  in Eq. (14) is replaced with corresponding vector parameter:  $\mathbf{R} \equiv (\mathbf{R}_1, \dots, \mathbf{R}_{N_u})^T$ . Then, one can define the following adiabatic electronic states and eigenvalues:

$$\hat{H}_{en}(\mathbf{R})|\psi_{e,j}(\mathbf{R})\rangle = E_{e,j}(\mathbf{R})|\psi_{e,j}(\mathbf{R})\rangle, \quad (16)$$

where  $j$  denotes collectively the set of all quantum numbers needed to completely define all the electronic states. Thus, the following completeness relation holds in the electronic space:

$$\hat{1}_e = \sum_j |\psi_{e,j}(\mathbf{R})\rangle \langle \psi_{e,j}(\mathbf{R})|. \quad (17)$$

It is possible to express  $\hat{H}$  in the basis of the above adiabatic electronic states,<sup>5</sup> which naturally result in the following decomposition of the Hamiltonian into adiabatic and non-adiabatic terms as follows:

$$\hat{H} = \hat{H}_{ad} + \frac{\hbar}{2} \sum_{\alpha} \left( \hat{P}_{\alpha} \hat{F}_{\alpha} + \hat{F}_{\alpha} \hat{P}_{\alpha} \right) + \hbar^2 \hat{S}, \quad (18)$$

where  $\hat{H}_{ad}$  is the adiabatic approximation given by

$$\hat{H}_{ad} = \int d\mathbf{R} \sum_k |\mathbf{R}\rangle \langle \psi_{e,k}(\mathbf{R})| \left\{ - \sum_{\alpha} \frac{\hbar^2}{2M_{\alpha}} \frac{\partial^2}{\partial R_{\alpha}^2} + U_k(\mathbf{R}) \right\} \langle \psi_{e,k}(\mathbf{R})| \langle \mathbf{R}|, \quad (19)$$

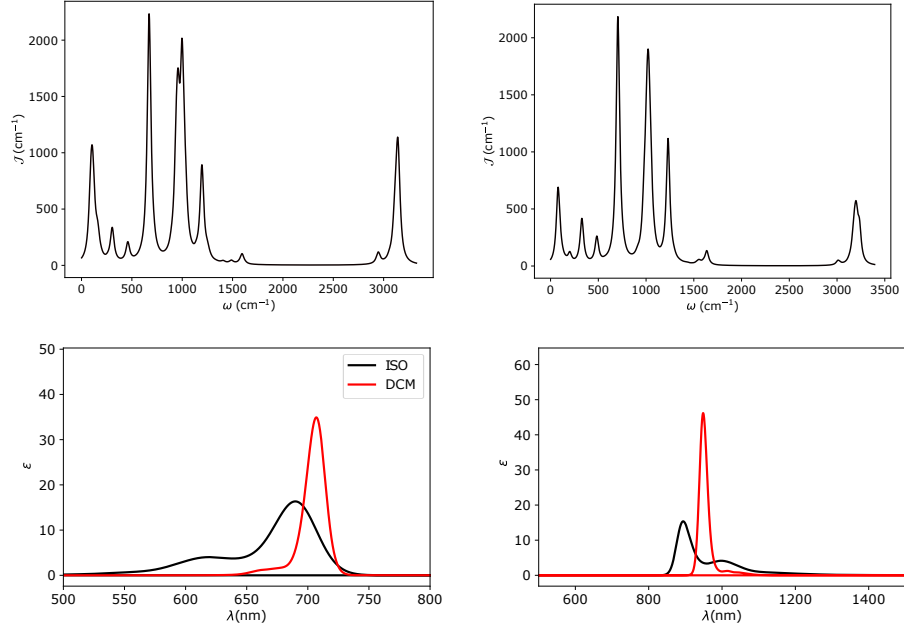


FIG. 10. Spectral densities,  $\mathcal{J}_{10}(\omega)$  and  $\mathcal{J}_{01}(\omega)$  (upper panels), and absorption and emission line shapes (lower panels) of Flav5 molecule in PCM solvent model. Lineshapes for isolated molecules are also shown for comparison.

with  $U_k(\mathbf{R}) = E_{e,k}(\mathbf{R}) + \frac{1}{2} \sum_{c=1}^{N_u} \sum_{c' \neq c} \frac{Z_c Z_{c'}}{|\mathbf{R}_c - \mathbf{R}_{c'}|}$  and  $\alpha$  denoting each one dimensional cartesian direction of a nucleus. Thus,  $\alpha = 1, \dots, 3N_u$ . In Eq. (18),  $\hat{P}_\alpha$  is the nuclear momentum operator along each direction,  $\hat{F}_\alpha$  is the first derivative nonadiabatic coupling term, and  $\hat{S}$  is the second derivative nonadiabatic coupling term. In more detail, these derivative coupling terms can be expressed as<sup>5</sup>

$$\hat{F}_\alpha = \int d\mathbf{R} \sum_k \sum_{k'} |\mathbf{R}\rangle \langle \psi_{e,k}(\mathbf{R}) | F_{\alpha,kk'}(\mathbf{R}) \langle \psi_{e,k'}(\mathbf{R}) | \langle \mathbf{R} |, \quad (20)$$

$$\hat{S} = \int d\mathbf{R} \sum_k \sum_{k'} |\mathbf{R}\rangle \langle \psi_{e,k}(\mathbf{R}) | S_{kk'}(\mathbf{R}) \langle \psi_{e,k'}(\mathbf{R}) | \langle \mathbf{R} |, \quad (21)$$

where

$$F_{\alpha,kk'}(\mathbf{R}) = -\frac{i}{M_\alpha} \langle \psi_{e,k}(\mathbf{R}) | \left( \frac{\partial}{\partial R_\alpha} | \psi_{e,k'}(\mathbf{R}) \rangle \right), \quad (22)$$

$$S_{kk'}(\mathbf{R}) = \frac{1}{2} \sum_\alpha \sum_{k''} M_\alpha F_{\alpha,kk''}(\mathbf{R}) F_{\alpha,k''k'}(\mathbf{R}). \quad (23)$$

For the case  $k \neq k'$  and  $E_{e,k}(\mathbf{R})$  and  $E_{e,k'}(\mathbf{R})$  are non-degenerate, the Hellmann-Feynman theorem<sup>6,7</sup> can be used to obtain an alternative expression for  $F_{\alpha,kk'}(\mathbf{R})$ , which is obtained by taking derivative of the following condition:

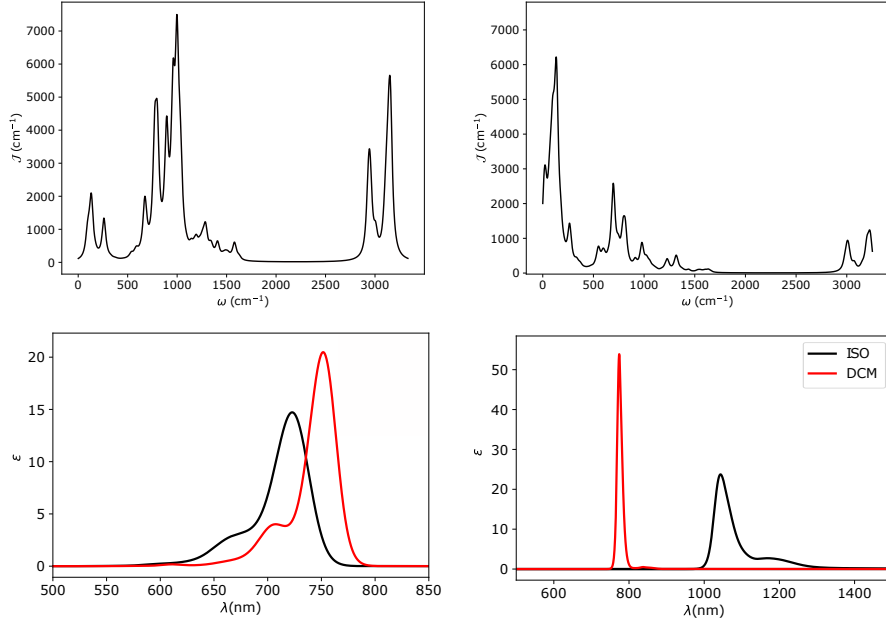


FIG. 11. Spectral densities,  $\mathcal{J}_{10}(\omega)$  and  $\mathcal{J}_{01}(\omega)$  (upper panels), and absorption and emission line shapes (lower panels) of Flav7 molecule in PCM solvent model. Lineshapes for isolated molecules are also shown for comparison.

$\langle \psi_{e,k}(\mathbf{R}) | \hat{H}_e(\mathbf{R}) | \psi_{e,k'}(\mathbf{R}) \rangle = E_{e,k}(\mathbf{R}) \delta_{kk'}$ . The resulting expression is

$$F_{\alpha,kk'}(\mathbf{R}) = \frac{i}{M_\alpha} \frac{\langle \psi_{e,k}(\mathbf{R}) | \left( \frac{\partial \hat{H}_e(\mathbf{R})}{\partial R_\alpha} \right) | \psi_{e,k'}(\mathbf{R}) \rangle}{E_{e,k}(\mathbf{R}) - E_{e,k'}(\mathbf{R})}. \quad (24)$$

Let us now consider the case where there are two major adiabatic electronic states with significant nonadiabatic couplings, which we denote as 1 and 2. Then, the adiabatic Hamiltonian including the diagonal components of the second derivative nonadiabatic terms can be expressed as

$$\begin{aligned} \hat{H}_{ad} + \hbar^2 \hat{S} = & \int d\mathbf{R} |\mathbf{R}\rangle |\psi_{e,1}(\mathbf{R})\rangle \left\{ - \sum_{\alpha} \frac{\hbar^2}{2M_{\alpha}} \frac{\partial^2}{\partial R_{\alpha}^2} + U_1(\mathbf{R}) + S_{11}(\mathbf{R}) \right\} \langle \psi_{e,1}(\mathbf{R}) | \langle \mathbf{R} | \\ & + \int d\mathbf{R} |\mathbf{R}\rangle |\psi_{e,2}(\mathbf{R})\rangle \left\{ - \sum_{\alpha} \frac{\hbar^2}{2M_{\alpha}} \frac{\partial^2}{\partial R_{\alpha}^2} + U_2(\mathbf{R}) + S_{22}(\mathbf{R}) \right\} \langle \psi_{e,2}(\mathbf{R}) | \langle \mathbf{R} | \end{aligned} \quad (25)$$

Assuming that all  $\langle \mathbf{r} | \psi_{e,k}(\mathbf{R}) \rangle$ 's are real valued functions,  $F_{\alpha,11}(\mathbf{R}) = F_{\alpha,22}(\mathbf{R}) = 0$ . As a result,  $S_{12}(\mathbf{R}) = S_{21}(\mathbf{R}) = 0$ . Thus, the only terms that couple the two adiabatic electronic states are the first derivative nonadiabatic terms as follows:

$$\hat{H}_c = \frac{\hbar}{2} \sum_{\alpha} \left( \hat{P}_{\alpha} \hat{F}_{\alpha} + \hat{F}_{\alpha} \hat{P}_{\alpha} \right), \quad (26)$$

where

$$\hat{F}_{\alpha} = \int d\mathbf{R} |\mathbf{R}\rangle \left( F_{\alpha,12}(\mathbf{R}) |\psi_{e,1}(\mathbf{R})\rangle \langle \psi_{e,2}(\mathbf{R})| + F_{\alpha,21}(\mathbf{R}) |\psi_{e,2}(\mathbf{R})\rangle \langle \psi_{e,1}(\mathbf{R})| \right) \langle \mathbf{R} |. \quad (27)$$

Note that  $F_{\alpha,12}(\mathbf{R}) = [F_{\alpha,21}(\mathbf{R})]^*$ , which makes the above operator Hermitian.

Let us assume that the initial state is near the minimum energy nuclear coordinates of the  $E_{e,1}(\mathbf{R})$ , which is denoted as  $\mathbf{R}_1^*$  and that the adiabatic electronic states in this vicinity can be approximated as those for the particular nuclear coordinates, which are respectively denoted as  $|\psi_{k,e}\rangle = |\psi_{k,e}(\mathbf{R}_1^*)\rangle$ . Then, the adiabatic Hamiltonian can be

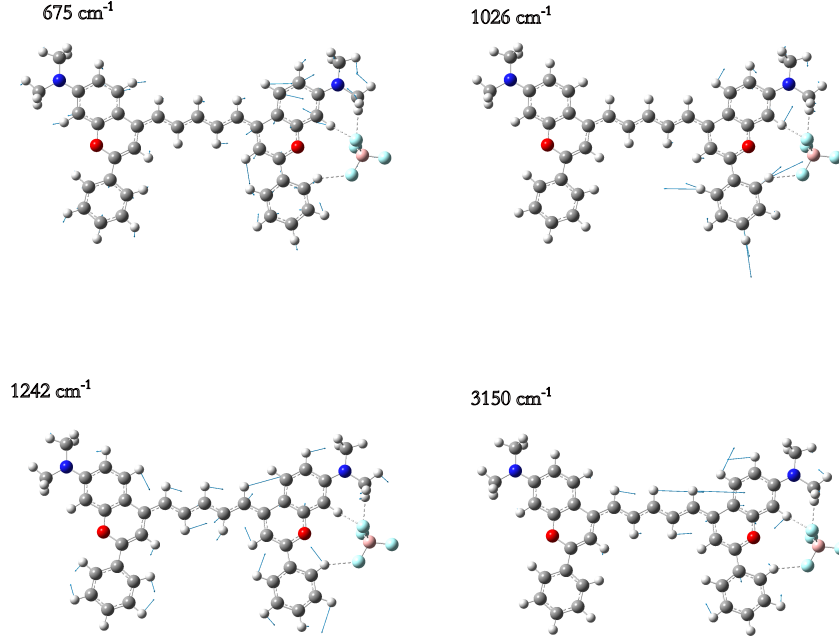


FIG. 12. Displacement vectors for the main vibrational modes contributing to the line shape representation of Flav5 molecule.

approximated as<sup>5</sup>

$$\begin{aligned} \hat{H}_{ad} + \hbar^2 \hat{S} \approx & \left\{ \sum_{\alpha} \frac{\hat{P}_{\alpha}^2}{2M_{\alpha}} + U_1(\hat{\mathbf{R}}) + S_{11}(\mathbf{R}_1^*) \right\} |\psi_{e,1}\rangle \langle \psi_{e,1}| \\ & + \left\{ \sum_{\alpha} \frac{\hat{P}_{\alpha}^2}{2M_{\alpha}} + U_2(\hat{\mathbf{R}}) + S_{22}(\mathbf{R}_1^*) \right\} |\psi_{e,2}\rangle \langle \psi_{e,2}|, \end{aligned} \quad (28)$$

and the first derivative nonadiabatic coupling operator  $\hat{F}_{\alpha}$  in Eq. (26) can be approximated as

$$\hat{F}_{\alpha} \approx F_{\alpha,12}(\mathbf{R}_1^*) |\psi_{e,1}\rangle \langle \psi_{e,2}| + F_{\alpha,21}(\mathbf{R}_1^*) |\psi_{e,2}\rangle \langle \psi_{e,1}|. \quad (29)$$

Let us introduce mass weighted coordinates  $\tilde{R}_{\alpha} = \sqrt{M_{\alpha}} R_{\alpha}$  and the corresponding canonical momentum,  $\tilde{P}_{\alpha} = P_{\alpha} / \sqrt{M_{\alpha}}$ . Then, Eqs. (28) can be expressed as

$$\begin{aligned} \hat{H}_{ad} + \hbar^2 \hat{S} \approx & \left\{ \sum_{\alpha} \frac{\hat{P}_{\alpha}^2}{2} + U_1(\hat{\mathbf{R}}) + \mathbf{S}_{11}(\tilde{\mathbf{R}}_1^*) \right\} |\psi_{e,1}\rangle \langle \psi_{e,1}| \\ & + \left\{ \sum_{\alpha} \frac{\hat{P}_{\alpha}^2}{2} + U_2(\hat{\mathbf{R}}) + \mathbf{S}_{22}(\tilde{\mathbf{R}}_1^*) \right\} |\psi_{e,2}\rangle \langle \psi_{e,2}|, \end{aligned} \quad (30)$$

Similarly,  $F_{\alpha,12}(\mathbf{R}_1^*)$  in Eq. (29) can be expressed as

$$F_{\alpha,12} = \frac{i}{\sqrt{M_{\alpha}}} \frac{\langle \psi_{e,1} | \left( \partial \hat{H}_e(\tilde{\mathbf{R}}) / \partial \tilde{R}_{\alpha} \right) |_{\mathbf{R}=\mathbf{R}_1^*} \psi_{e,2} \rangle}{E_{e,1}(\mathbf{R}_1^*) - E_{e,2}(\mathbf{R}_1^*)}. \quad (31)$$

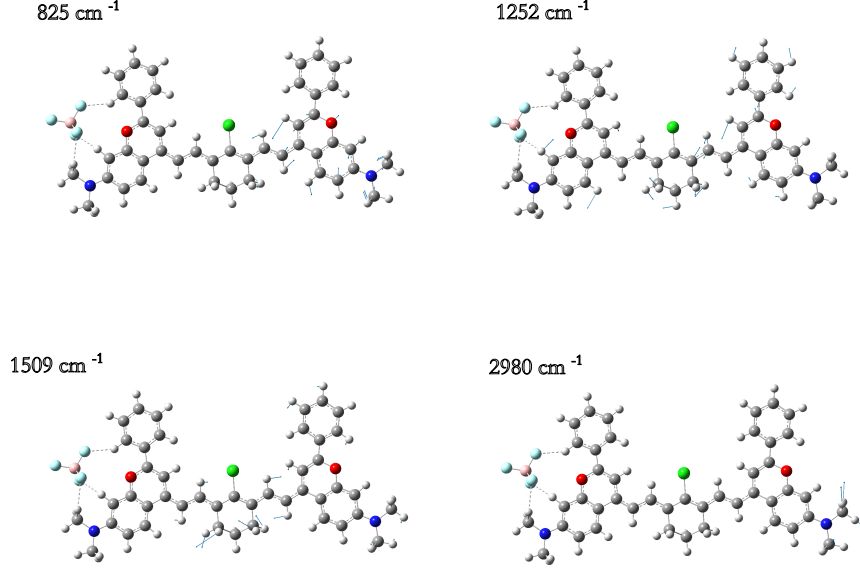


FIG. 13. Displacement vectors for the main vibrational modes contributing to the line shape representation of Flav7 molecule.

Expanding  $U_1(\hat{\mathbf{R}})$  around  $\mathbf{R}_1^*$  up to the second order and diagonalizing the Hessian matrix, we can introduce the following normal coordinates:

$$q_j = \sum_{\alpha} L_{1,j\alpha} (\tilde{R}_{\alpha} - \tilde{R}_{1,\alpha}^*) = \sum_{\alpha} L_{1,j\alpha} \sqrt{M_{\alpha}} (R_{\alpha} - R_{1,\alpha}^*), j = 1, \dots, N_v, \quad (32)$$

with  $N_v$  being the total number of normal mode vibrations. Let us denote the corresponding canonical momentum as  $p_j$ . Then,

$$\sum_{\alpha} \frac{\hat{P}_{\alpha}^2}{2} + U_1(\hat{\mathbf{R}}) \approx \sum_j \left( \frac{1}{2} \hat{p}_j^2 + \frac{\omega_j^2}{2} \hat{q}_j^2 \right) + U_1(\mathbf{R}_1^*), \quad (33)$$

$$\begin{aligned} \hat{H}_c &= \hbar \sum_{\alpha} \sum_j \sum_{j'} L_{1,j\alpha} L_{1,j'\alpha} \hat{p}_j \left\{ F_{j',12} |\psi_{e,1}\rangle \langle \psi_{e,2}| + F_{j',21} |\psi_{e,2}\rangle \langle \psi_{e,1}| \right\} \\ &= \hbar \sum_j \hat{p}_j \left\{ F_{j,12} |\psi_{e,1}\rangle \langle \psi_{e,2}| + F_{j,21} |\psi_{e,2}\rangle \langle \psi_{e,1}| \right\}, \end{aligned} \quad (34)$$

where

$$\begin{aligned} F_{j,12} &= i \frac{\langle \psi_{e,1} | \left( \frac{\partial \hat{H}_e(\mathbf{R})}{\partial q_j} \Big|_{\mathbf{R}=\mathbf{R}_1^*} \right) | \psi_{e,2} \rangle}{E_{e,1}(\mathbf{R}_1^*) - E_{e,2}(\mathbf{R}_1^*)} \\ &= i \sum_{\alpha} \frac{L_{1,j\alpha}}{\sqrt{M_{\alpha}}} \frac{\langle \psi_{e,1} | \left( \frac{\partial \hat{H}_e(\mathbf{R})}{\partial R_{\alpha}} \Big|_{\mathbf{R}=\mathbf{R}_1^*} \right) | \psi_{e,2} \rangle}{E_{e,1}(\mathbf{R}_1^*) - E_{e,2}(\mathbf{R}_1^*)}. \end{aligned} \quad (35)$$

Equation (34) shows that the first derivative non-adiabatic coupling term still includes momentum operator along each normal mode even within the crude adiabatic approximation. For the purpose of using Fermi's golden rule within the Condon approximation, an average value of the coupling as defined below can be used.

$$\hat{H}_c \approx \hbar \left( \sum_j \langle \hat{p}_j^2 \rangle^{1/2} |F_{j,12}| \right) (|\psi_{e,1}\rangle \langle \psi_{e,2}| + |\psi_{e,2}\rangle \langle \psi_{e,1}|). \quad (36)$$

where  $\langle \hat{p}_j^2 \rangle$  is the thermal average over the distribution of vibrational states for the initial electronic state.

For the case of nonradiative decay from  $S_1$  to  $S_0$ ,  $|\psi_{e,1}\rangle = |\tilde{S}_1\rangle$ ,  $|\psi_{e,2}\rangle = |S_0\rangle$ ,  $E_{e,1}(\mathbf{R}_1^*) = \tilde{E}_1$ , and  $E_{e,2}(\mathbf{R}_1^*) = E_0$ , Eq. (34) is expressed as

$$\hat{H}_c \approx \hbar \left( \sum_j \langle \hat{p}_j^2 \rangle^{1/2} \frac{\left| \sum_\alpha \frac{L_{1,j\alpha}}{\sqrt{M_\alpha}} \langle \tilde{S}_1 | \left( \frac{\partial \hat{H}_e(\mathbf{R})}{\partial R_\alpha} \Big|_{\mathbf{R}=\mathbf{R}_1^*} \right) |S_0\rangle \right|}{\tilde{E}_1 - E_0} \right) (|\tilde{S}_1\rangle \langle S_0| + |S_0\rangle \langle \tilde{S}_1|). \quad (37)$$

In this work, the matrix element of  $\partial \hat{H}_e(\mathbf{R}) / \partial q_j$  in the above equation is calculated within the adiabatic linear response TD-DFT method. The detailed ansatz used for deriving the expression can be found in the literature<sup>8,9</sup>.

#### D. Duschinsky matrix elements

For further examination of detailed vibronic channels involved in the nonadiabatic transition from  $S_1$  to  $S_0$ , we also calculated the Duschinsky rotation matrix<sup>10–12</sup> from the displacement of the nuclei in the normal modes. Let us denote the vector of normal mode vibrational coordinates for  $S_1$  as  $\mathbf{q}_1$  and that for  $S_0$  as  $\mathbf{q}_2$ , which are assumed to be determined in a common frame of reference that satisfy the Eckart conditions.<sup>10,13,14</sup> Then,

$$\mathbf{q}_1 = \mathbf{L}_1(\tilde{\mathbf{R}} - \tilde{\mathbf{R}}_1^*) \quad (38)$$

$$\mathbf{q}_0 = \mathbf{L}_0(\tilde{\mathbf{R}} - \tilde{\mathbf{R}}_0^*) \quad (39)$$

where  $\tilde{\mathbf{R}}_1^*$  and  $\tilde{\mathbf{R}}_0^*$  are mass-weighted nuclear coordinates where the potential energies of  $S_1$  and  $S_0$  are minimum respectively. Employing the relationship,  $\tilde{\mathbf{R}} = \mathbf{L}_0^T \mathbf{q}_0 + \tilde{\mathbf{R}}_0^*$ , which corresponds to the inverse of Eq. (39), in Eq. (38), we obtain

$$\begin{aligned} \mathbf{q}_1 &= \mathbf{L}_1 \mathbf{L}_0^T \mathbf{q}_0 + \mathbf{L}_1(\tilde{\mathbf{R}}_0^* - \tilde{\mathbf{R}}_1^*) \\ &= \mathbf{J}_{10} \mathbf{q}_0 + \mathbf{D}_{10}, \end{aligned} \quad (40)$$

where the first line defines the Duschinsky rotation matrix  $\mathbf{J}_{10}$  and the displacement vector  $\mathbf{D}_{10}$  shown in the second line. Figures 14 and 15 show the Duschinsky rotation matrices for Flav5 and Flav7 respectively.

#### E. Nonadiabatic rates for transition to triplet states

The major coupling responsible for the transition between singlet and triplet states is the spin-orbit coupling, which, for TD-DFT states, can be expressed using the one-electron Breit Pauli Hamiltonian<sup>15,16</sup> as follows:

$$\hat{H}_{SO} = -\frac{\alpha_0^2}{2} \sum_{i,c} \frac{Z_c}{r_{ic}^3} (\hat{\mathbf{r}}_{ic} \times \hat{\mathbf{p}}_i) \cdot \hat{s}_i, \quad (41)$$

where  $\alpha_0 = 137.037^{-1}$  is the fine structure constant,  $\hat{\mathbf{r}}_{ic}$ ,  $\hat{\mathbf{p}}_i$  and  $\hat{s}_i$  are the position (with respect to nucleus labeled as  $c$ ), momentum, and spin operators of electron  $i$ , and  $Z_c$  is the nuclear charge. Employing the second quantization representation, the Hamiltonian  $\hat{H}_{SO}$  takes the following form:

$$\hat{H}_{SO_x} = -\frac{\alpha_0^2}{2} \sum_{p,q} \tilde{L}_{xpq} \cdot \frac{\hbar}{2} (a_{p_\alpha}^\dagger a_{q_\beta} - a_{p_\beta}^\dagger a_{q_\alpha}), \quad (42)$$

$$\hat{H}_{SO_y} = -\frac{\alpha_0^2}{2} \sum_{p,q} \tilde{L}_{ypq} \cdot \frac{\hbar}{2} (a_{p_\alpha}^\dagger a_{q_\beta} - a_{p_\beta}^\dagger a_{q_\alpha}), \quad (43)$$

$$\hat{H}_{SO_z} = -\frac{\alpha_0^2}{2} \sum_{p,q} \tilde{L}_{zpq} \cdot \frac{\hbar}{2} (a_{p_\alpha}^\dagger a_{q_\alpha} - a_{p_\beta}^\dagger a_{q_\beta}), \quad (44)$$

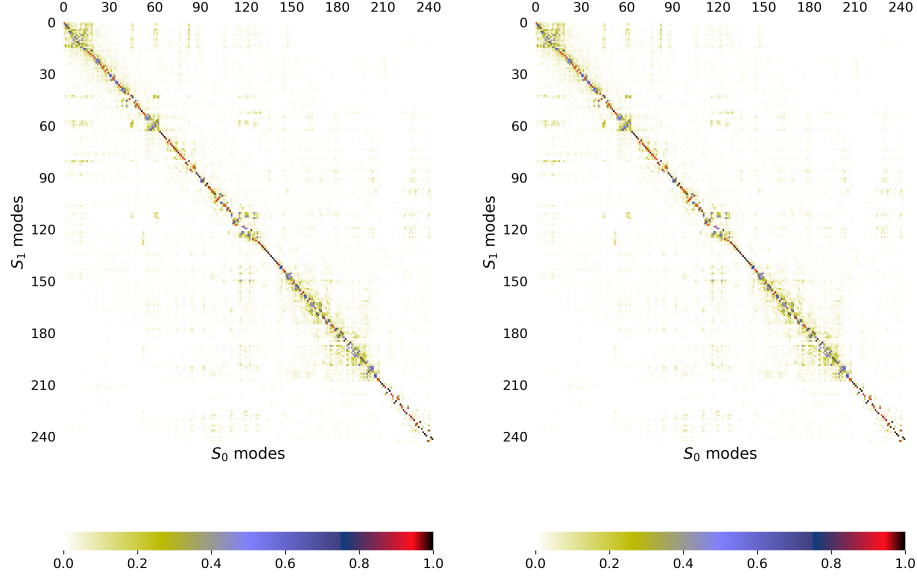


FIG. 14. Duschinsky matrix between the normal modes for the Flav5 dye for the two types of systems, isolated (left), and deuterated (right).

where  $p$  and  $q$  represent molecular orbital indices,  $\alpha$  and  $\beta$  respectively denote spin up and down, Finally,  $\tilde{L}_{\mu pq}$ , with  $\mu = x, y,$  and  $z,$  represents component of the matrix element (with respect to  $p$  and  $q$  orbitals) of the operator  $\sum_{i,c} Z_c \hat{\mathbf{L}}_{ic} / r_{ic}^3$ , where  $\hat{\mathbf{L}}_{ic} = \hat{\mathbf{r}}_{ic} \times \hat{\mathbf{p}}_i$ . On the other hand, the single reference excited states within the Tamm-Dancoff approximation<sup>17</sup> are expressed as

$$|\Phi_{singlet}^I\rangle = \sum_{i,a} s_i^{Ia} (a_{a\alpha}^\dagger a_{i\alpha} - a_{a\beta}^\dagger a_{i\beta}) |\Phi_{HF}\rangle \quad (45)$$

$$|\Phi_{triplet}^{I,m_s=0}\rangle = \sum_{i,a} t_i^{Ia} (a_{a\alpha}^\dagger a_{i\alpha} - a_{a\beta}^\dagger a_{i\beta}) |\Phi_{HF}\rangle \quad (46)$$

$$|\Phi_{triplet}^{I,m_s=1}\rangle = \sum_{i,a} \sqrt{2} t_i^{Ia} a_{a\alpha}^\dagger a_{i\beta} |\Phi_{HF}\rangle \quad (47)$$

$$|\Phi_{triplet}^{I,m_s=-1}\rangle = \sum_{i,a} \sqrt{2} t_i^{Ia} a_{a\beta}^\dagger a_{i\alpha} |\Phi_{HF}\rangle \quad (48)$$

where  $s_i^{Ia}$  and  $t_i^{Ia}$  are the singlet and triplet excitation coefficients for the  $I^{th}$  singlet or triplet excitation. We use  $i, j$  to denote occupied orbitals, and  $a, b$  to denote virtual orbitals. These excitations evolve from  $|\Phi_{HF}\rangle$ , the reference Hartree-Fock ground state. Combining all the terms defined above, we can express the spin-orbit coupling as follows:<sup>18,19</sup>

$$\langle \Phi_{singlet}^I | \hat{H}_{SO} | \Phi_{triplet}^{J,m_s=0} \rangle = \frac{\alpha_0^2 \hbar}{2} \left( \sum_{i,a,b} \tilde{L}_{zab} s_i^{Ia} t_i^{Jb} - \sum_{i,j,a} \tilde{L}_{zij} s_i^{Ia} t_j^{Ja} \right), \quad (49)$$

$$\begin{aligned} \langle \Phi_{singlet}^I | \hat{H}_{SO} | \Phi_{triplet}^{J,m_s=\pm 1} \rangle = & \pm \frac{\alpha_0^2 \hbar}{2\sqrt{2}} \left( \sum_{i,a,b} \tilde{L}_{xab} s_i^{Ia} t_i^{Jb} - \sum_{i,j,a} \tilde{L}_{xij} s_i^{Ia} t_j^{Ja} \right) \\ & + \frac{\alpha_0^2 \hbar}{2\sqrt{2}i} \left( \sum_{i,a,b} \tilde{L}_{yab} s_i^{Ia} t_i^{Jb} - \sum_{i,j,a} \tilde{L}_{yij} s_i^{Ia} t_j^{Ja} \right). \end{aligned} \quad (50)$$



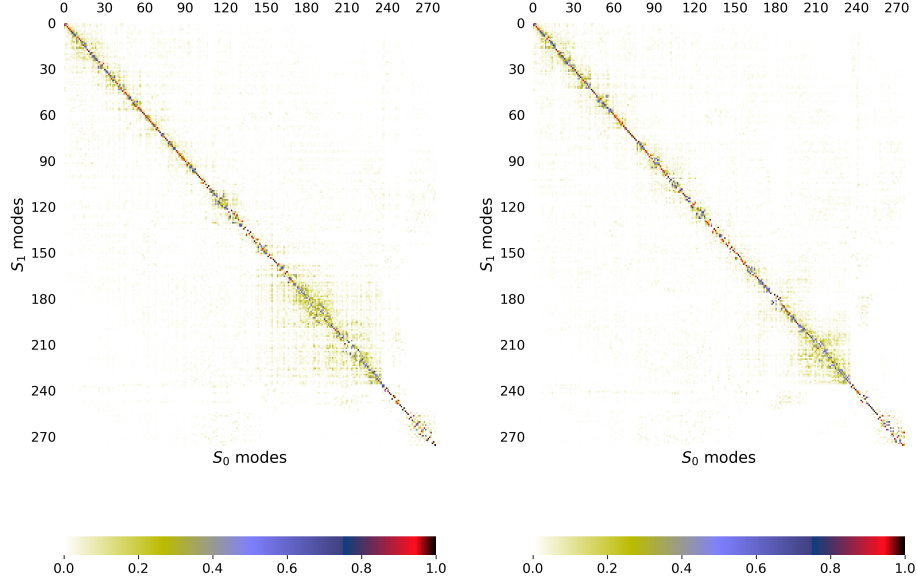


FIG. 15. Duschinsky matrix between normal modes for the Flav7 dye for the two types of systems, isolated (left), and deuterated (right).

Finally, the net spin-orbit coupling is obtained as the root mean squared of the different contributions as follows:

$$\langle \Phi_{singlet}^I | \hat{H}_{SO} | \Phi_{triplet}^J \rangle = \sqrt{\sum_{m_s=0,\pm 1} \|\langle \Phi_{singlet}^I | \hat{H}_{SO} | \Phi_{triplet}^{I,m_s} \rangle\|^2} \quad (51)$$

The resulting singlet-triple transition rates versus the energy gap are shown in Figs. 16) and 17.

## F. Experimental lifetime measurements

The standard procedure for all the lifetime measurements is as follows: We recorded PL lifetimes using a home-built, all-reflective epifluorescence setup.<sup>20</sup> For all dyes below we used a pulsed 785 nm excitation. Emission was then collected and filtered with a 90:10 beamsplitter and appropriate excitation filters finally reflectively coupled into a single-mode fiber (F-SMF-28-C-10FC, Newport) and detected using an SNSPD (Quantum Opus One).<sup>20-22</sup> Given the short lifetimes of these dyes, lifetimes were fit with a convolution of the instrument response function and an exponential. To determine the lifetime (or decay rate,  $k$ ) for each TCSPC trace we fit each curve to a convolution of the sum of two Gaussians with a single exponential decay:

$$I(t) = \frac{I_0}{2} \exp \left\{ -k \left( (t - t_0) - \frac{\sigma_1^2 k}{2} \right) \right\} \left\{ 1 + \operatorname{erf} \left( \frac{(t - t_0) - \sigma_1^2 k}{\sqrt{2}\sigma_1} \right) \right\} + \frac{aI_0}{2} \exp \left\{ -k \left( (t - t_0 - t_1) - \frac{\sigma_2^2 k}{2} \right) \right\} \left\{ 1 + \operatorname{erf} \left( \frac{(t - t_0 - t_1) - \sigma_2^2 k}{\sqrt{2}\sigma_2} \right) \right\} \quad (52)$$

The width,  $\sigma_1$  and  $\sigma_2$  of each Gaussian, the time offset,  $t_1$ , between the two Gaussians and amplitude scale,  $\alpha$ , were determined using the instrument response function (IRF) which was measured as the backscatter off of a cuvette with solvent (e.g.,DCM) without the longpass filters (Table IF). The initial peak amplitude,  $I_0$ , the rate,  $k$ , and  $t_0$  were free fitting parameters, while the time offset,  $t_1$ , and the IRF widths,  $\sigma_1$  and  $\sigma_2$  were fixed variables. We use a conservative error of 1 ps (the instrument resolution) for our lifetimes.

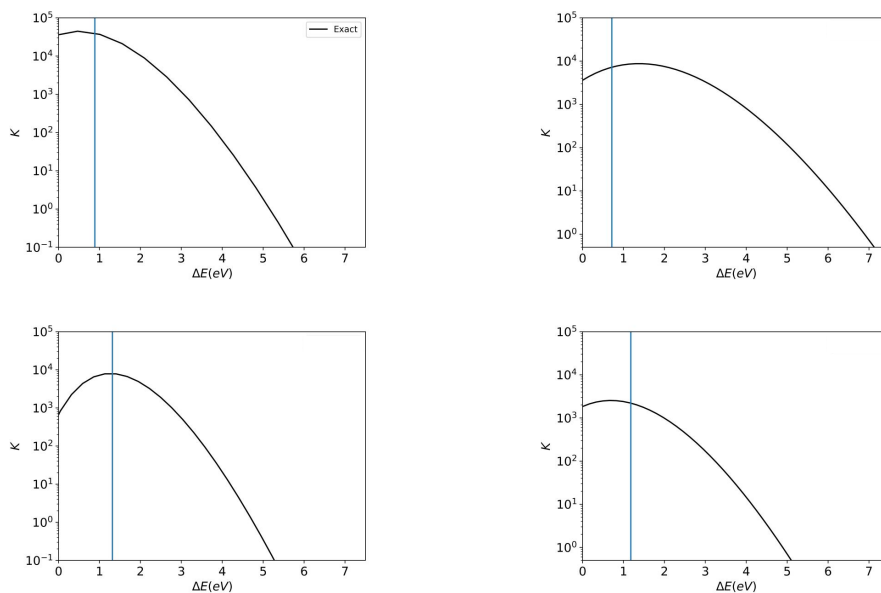


FIG. 16. Nonadiabatic transition rates (in logarithmic scale) versus energy gap calculated for the electronic transition in both Flav5 (left column) and Flav7 (right column) dyes. The computed transitions from top to bottom are:  $T_1 \rightarrow S_0$  and  $T_2 \rightarrow S_0$  respectively. The vertical line represents the corresponding energy gap between the coupled states.

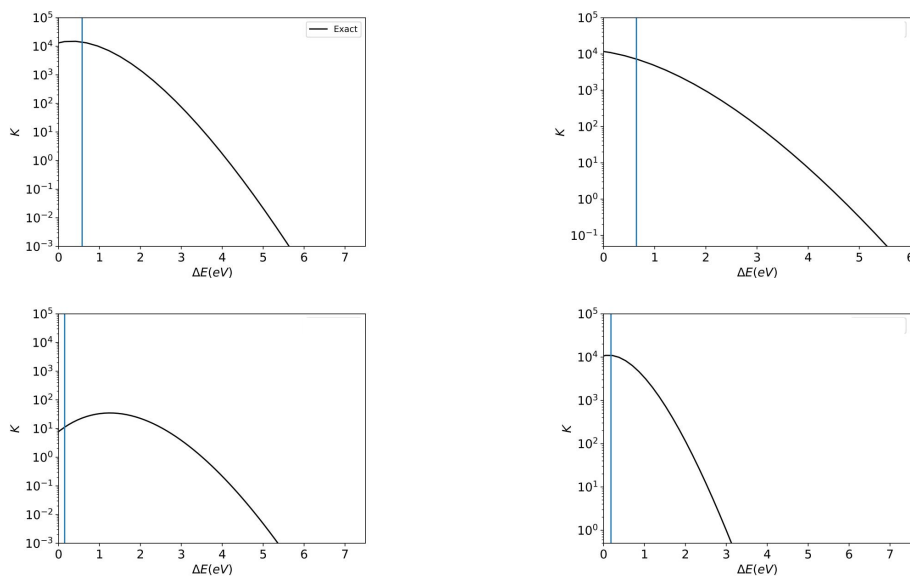


FIG. 17. Nonadiabatic transition rates (in logarithmic scale) versus energy gap calculated for the electronic transition in both Flav5 (left column) and Flav7 (right column) dyes. The computed transitions from top to bottom are:  $T_1 \rightarrow S_1$  and  $T_2 \rightarrow S_1$  respectively. The vertical line represents the corresponding energy gap between the coupled states.

TABLE IV. Parameters used for IRF fit.

IRF fit parameters	Numerical values for the fit
$\sigma_1$ (ps)	32.0
$\sigma_2$ (ps)	50.6
$t_1$ (ps)	6.6
$\alpha$	1.6

## G. Information on Materials and general experimental procedures

### 1. Materials

Chemical reagents were purchased from Accela, Acros Organics, Alfa Aesar, Carl Roth, Fisher Scientific, Sigma-Aldrich, or TCI and used without purification. Anhydrous solvents and deoxygenated solvents (toluene, acetonitrile, dimethylformamide, THF) were obtained from a Grubb’s-type Phoenix Solvent Drying System constructed by JC Meyer. Anhydrous solvents (1,4-dioxane, ethanol, n-butanol) were prepared by drying over 4 Åmolecular sieves for at least 3 days. Oxygen was removed from reaction mixtures by three consecutive freeze-pump-thaw cycles in air free glassware.

### 2. Instrumentation

Thin layer chromatography was performed using Silica Gel 60 F<sub>254</sub> (EMD Millipore) plates. Flash chromatography was executed with technical grade silica gel with 60 Å pores and 40–63 μm mesh particle size (Sorbtech Technologies). Solvent was removed under reduced pressure with a Büchi Rotovapor with a Welch self-cleaning dry vacuum pump and further dried with a Welch DuoSeal pump. Bath sonication was performed using a Branson 3800 ultrasonic cleaner. Microwave reactions were performed using a CEM Discover SP microwave synthesis reactor. Reactions were performed in glass 10 mL microwave reactor vials purchased from CEM with silicone/PTFE caps. Flea micro PTFE-coated stir bars were used in the vials with magnetic stirring set to high and 15 seconds of premixing prior to the temperature ramping. All <sup>1</sup>H and <sup>13</sup>C, spectra are reported in ppm and relative to residual solvent signals (<sup>1</sup>H and <sup>13</sup>C). Spectra were obtained on Bruker AV-300, AV-400, DRX-500, or AV-500 instruments and processed with MestReNova software. Liquid chromatography-mass spectrometry were obtained using an Agilent 6100 series quadrupole LC/MSD. Absorbance spectra were collected on a JASCO V-770 UV-Visible/NIR spectrophotometer with a 2000 nm/min scan rate after blanking with the appropriate solvent. Photoluminescence spectra were obtained on a Horiba Instruments PTI QuantaMaster Series fluorometer. Quartz cuvettes (1 cm) were used for absorbance and photoluminescence measurements. Absorption coefficients in DCM were calculated with serial dilutions with Hamilton syringes in volumetric glassware. Error was taken as the standard deviation of the triplicate experiments. Relative quantum yields were determined in DCM relative to IR-26 in DCM.

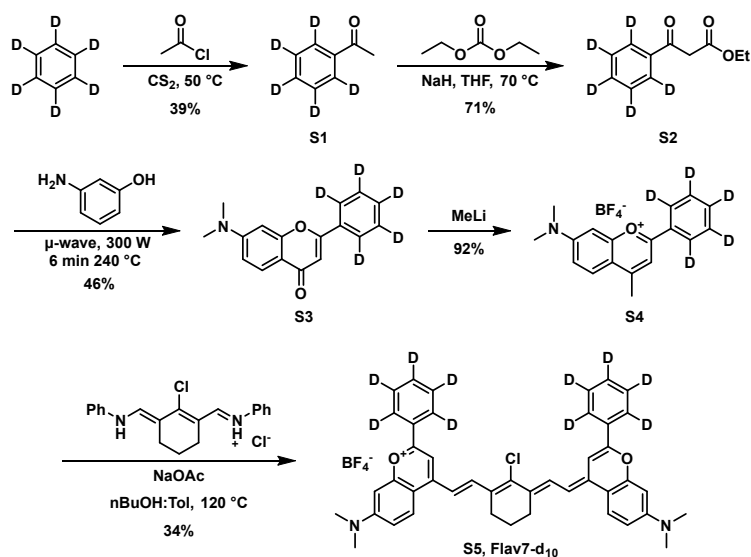
### 3. Abbreviations

DCM = dichloromethane; DMF = dimethylformamide; DMSO = dimethylsulfoxide; EtOH = ethanol; EtOAc = ethyl acetate; Et<sub>2</sub>O = diethyl ether; MeOH = methanol, Tol = toluene

## II. SYNTHETIC SCHEMES

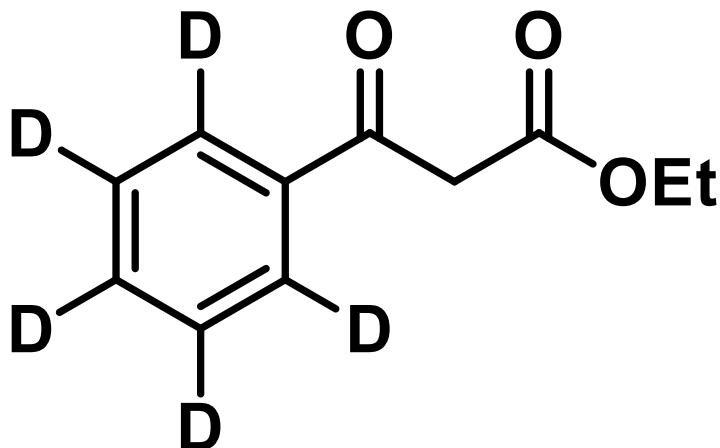
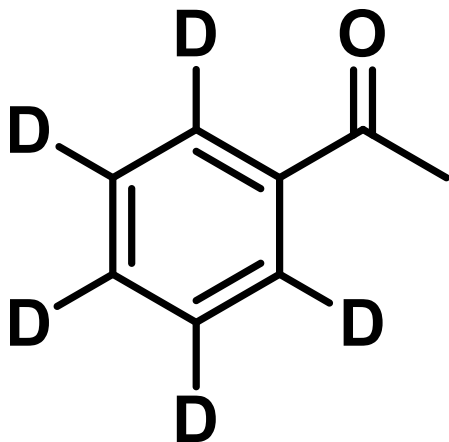
### III. SYNTHETIC PROCEDURES

**1-(phenyl-d<sub>5</sub>)ethan-1-one (S1):** Benzene-d<sub>6</sub> (550 μL, 5.94 mmol, 1.00 equiv.) and AlCl<sub>3</sub> (1.12 g, 7.72 mmol, 1.60 equiv.) were dissolved with 280 μL CS<sub>2</sub> in a dram vial. Acetyl chloride (570 μL, 7.72 mmol, 1.60 equiv.) dissolved in 500 μL CS<sub>2</sub> was added to the cloudy solution at 0 °C. After stirring for 5 hours at room temperature, the solution



was heated to 50 °C for 3 hours. The solution was cooled to 0 °C, quenched via dropwise addition of water and diluted (50 mL), extracted with DCM (3 x 75 mL), dried over Na<sub>2</sub>SO<sub>4</sub>, and concentrated. The pink oil was evaporated onto silica gel and purified via column chromatography with 9:1 Hex/EtOAc. The procedure afforded a pale yellow oil in 64% yield (468 mg, 3.71 mmol).  $R_f = 0.5$  in 9:1 Hex/EtOAc. <sup>1</sup>H NMR (500 MHz, CDCl<sub>3</sub>)  $\delta$  2.52 (s, 3H). <sup>13</sup>C NMR (126 MHz, CDCl<sub>3</sub>)  $\delta$  198.0, 136.9, 132.8 (t, J = 24.5 Hz), 128.4 (q, J = 11.3 Hz), 127.9 (t, J = 24.6 Hz), 76.9. HRMS (ESI<sup>+</sup>) calculated for C<sub>8</sub>H<sub>4</sub>D<sub>5</sub>O<sup>+</sup> [M+H]<sup>+</sup> : 126.0962; found: 126.0957.

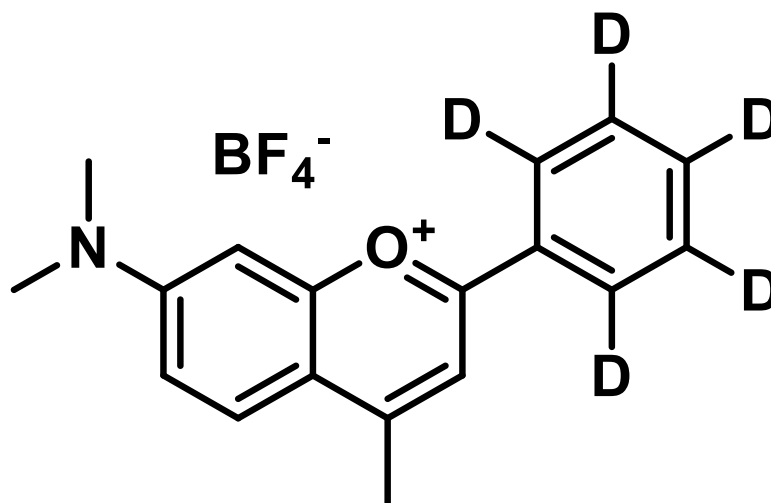
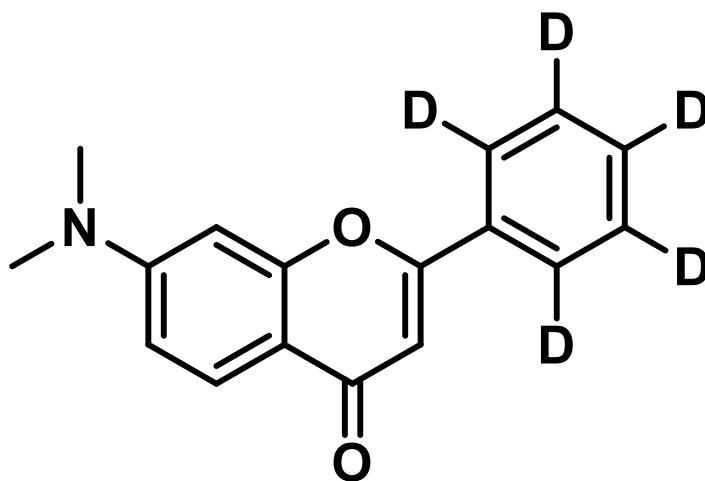
**ethyl 3-oxo-3-(phenyl-d<sub>5</sub>)propanoate (S2):** S1 (468 mg, 3.71 mmol, 1.00 equiv.), diethyl carbonate (1.8 mL, 15.3 mmol, 4.00 equiv.), and NaH (264 mg, 11.1 mmol, 3.00 equiv.) were dissolved with THF (4.6 mL, anhydrous) in a sealed synth vial. The reaction mixture was heated to 70 °C and stirred for 3 hours. The reaction was quenched with AcOH (100  $\mu$ L), diluted with water, extracted with EtOAc (3 x 50 mL), dried over Na<sub>2</sub>SO<sub>4</sub> and concentrated. The yellow oil was evaporated onto silica gel and purified via column chromatography with 9:1 Hex/EtOAc. The procedure resulted in a pale yellow oil in 71% yield (523 mg, 2.63 mmol).  $R_f = 0.4$  in 9:1 Hex/EtOAc. <sup>1</sup>H NMR (500



MHz, Acetonitrile- $d_3$ )  $\delta$  4.15 (m, 2H), 4.02 (s, 2H), 1.21 (m, 3H).  $^{13}\text{C}$  NMR (126 MHz,  $\text{CD}_3\text{CN}$ )  $\delta$  193.3, 167.7, 135.9, 133.2 (t,  $J = 24.7$  Hz), 128.2 (m), 128.0 (m), 61.0, 45.7, 13.4. HRMS (ESI $^+$ ) calculated for  $\text{C}_{11}\text{H}_8\text{D}_5\text{O}_3^+$   $[\text{M}+\text{H}]^+$  : 198.1173; found: 198.1156o.

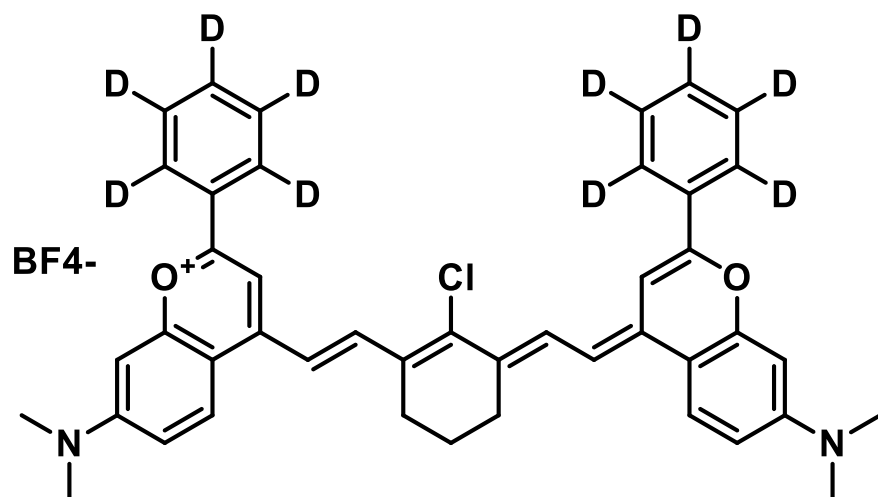
**7-(dimethylamino)-2-(phenyl- $d_5$ )-4H-chromen-4-one (S3):** **S2** (40 mg, 0.20 mmol, 2.0 equiv.) and 3-dimethylamino phenol (14 mg, 0.10 mmol, 1.0 equiv.) were added to a microwave reaction vial and heated for 6 minutes at 240 °C in a microwave reactor to produce a dark red oil. The crude mixture was evaporated onto silica gel and purified via column chromatography with a 9:1 to 0:1 gradient of Hex/EtOAc. The procedure yielded a dark brown solid in 46% yield (10 mg, 0.039 mmol).  $R_f = 0.3$  in 1:2 Hex/EtOAc.  $^1\text{H}$  NMR (500 MHz, Chloroform- $d$ )  $\delta$  8.01 (d,  $J = 9.0$  Hz, 1H), 6.73 (dd,  $J = 9.0, 2.5$  Hz, 1H), 6.67 (s, 1H), 6.55 (d,  $J = 2.5$  Hz, 1H), 3.07 (s, 6H).  $^{13}\text{C}$  NMR (126 MHz,  $\text{CDCl}_3$ )  $\delta$  177.8, 162.1, 158.3, 154.1, 132.1, 130.5 (t,  $J = 24.2$  Hz), 128.3 (t,  $J = 24.4$  Hz), 126.5, 125.6 (t,  $J = 24.9$  Hz), 113.6, 110.7, 107.2, 97.1, 40.1. HRMS (ESI $^+$ ) calculated for  $\text{C}_{17}\text{H}_{11}\text{D}_5\text{NO}_2^+$   $[\text{M}+\text{H}]^+$  : 271.1489; found: 271.1507.

**7-(dimethylamino)-4-methyl-2-(phenyl- $d_5$ )chromenylium (S4).** Compound **S3** (150 mg, 0.55 mmol, 1.0 equiv.) was added to a flame dried round bottom flask, dissolved with THF and cooled to 0 °C under  $\text{N}_2$  atmosphere. MeLi was added dropwise to the brown solution (690  $\mu\text{L}$  of 1.6 M solution in ether, 1.11 mmol, 2.00 equiv). After 30 minutes the solution was quenched with 50%  $\text{HBF}_4^-$  aqueous solution turning the solution red. The resulting solution was diluted with more 50%  $\text{HBF}_4^-$  aqueous solution (75 mL), extracted with DCM ( $3 \times 100\text{mL}$ ), dried over  $\text{Na}_2\text{SO}_4$  and concentrated. The red solid was then washed with boiling EtOAc (200 mL). The procedure yielded a dark red solid in 95% yield (141 mg, .520 mmol).  $^1\text{H}$  NMR (500 MHz,  $\text{CD}_2\text{Cl}_2$ )  $\delta$  8.06 (d,  $J = 9.6$  Hz, 1H), 7.70 (s, 1H), 7.37 (dd,  $J = 9.6, 2.5$  Hz, 1H), 7.03 (d,  $J = 2.5$  Hz, 1H), 3.39 (s, 6H), 2.91 (s, 3H).  $^{13}\text{C}$  NMR (126 MHz,  $\text{CD}_2\text{Cl}_2$ )



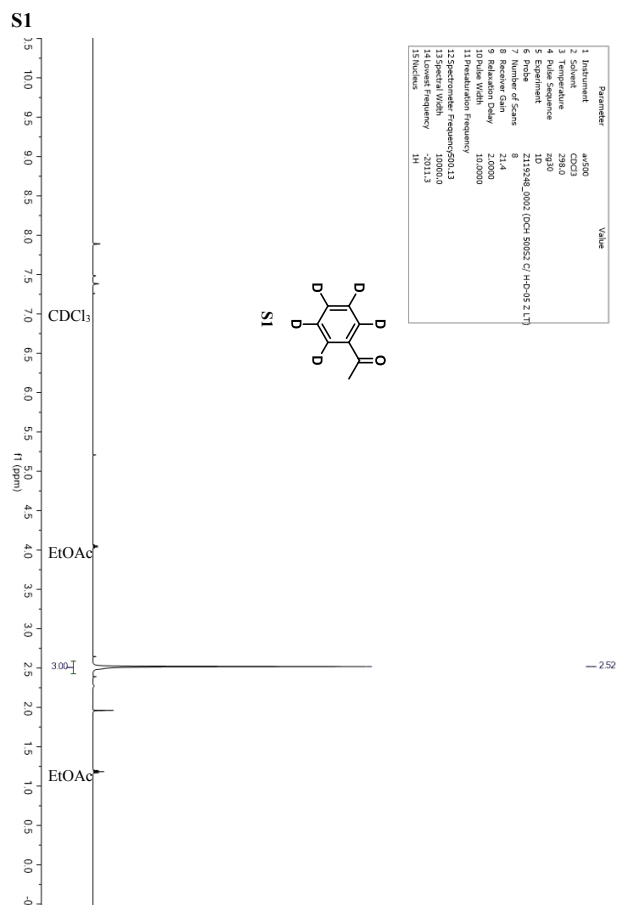
$\delta$  165.8, 163.6, 158.7, 157.9, 134.0 (t,  $J = 25.3$  Hz), 129.3 (t,  $J = 24.9$  Hz), 129.0, 128.5, 127.4 (t,  $J = 24.0$  Hz), 118.2, 117.9, 111.8, 96.1, 41.0, 19.9. HRMS (ESI<sup>+</sup>) calculated for C<sub>18</sub>H<sub>13</sub>D<sub>5</sub>NO<sup>+</sup> [M]<sup>+</sup>: 269.1617; found: 269.1677.

**4-((E)-2-((E)-2-chloro-3-(2-((E)-7-(dimethylamino)-2-(phenyl-d<sub>5</sub>)-4H-chromen-4-ylidene)ethylidene)cyclohex-1-en-1-yl)vinyl)-7-(dimethylamino)-2-(phenyl-d<sub>5</sub>) chromenylium (S5, Flav7-d10#).** Compound **S4** (80 mg, 0.30 mmol, 2.0 equiv.), N-[(3-(anilinomethylene)2-chloro-1-cyclohexen-1-yl)methylene]aniline hydrochloride, (48 mg, 0.15 mmol, 1.0 equiv.), and sodium acetate (74 mg, .90 mmol, 6.0 equiv.) were dissolved in n-butanol (1.2 mL) and toluene (0.61 mL) in a flame dried Schleck flask under N<sub>2</sub> atmosphere. The solution was freeze-pumped-thawed three times and heated to 100 °C for 45 min. The dark brown crude mixture was evaporated, loaded onto silica gel, and purified by column chromatography using a 0.5 to 10% DCM:EtOH gradient. The procedure yielded a dark burgundy solid in 34% yield (38 mg, 0.044 mmol).  $R_f = 0.5$  in 9:1 DCM:EtOH. <sup>1</sup>H NMR (500 MHz, DMSO-d<sub>6</sub>)  $\delta$  8.18 (d,  $J = 13.8$  Hz, 2H), 8.12 (d,  $J = 8.9$  Hz, 2H), 7.62 (s, 2H), 7.05 (d,  $J = 13.8$  Hz, 2H), 6.96 (d,  $J = 8.9$  Hz, 2H), 6.81 (s, 2H), 3.12 (s, 12H), 2.80 (s, 4H), 1.86 (s, 2H). HRMS (ESI<sup>+</sup>) calculated for C<sub>44</sub>H<sub>30</sub>D<sub>10</sub>ClN<sub>2</sub>O<sub>2</sub><sup>+</sup> [M]<sup>+</sup>: 673.3401; found: 673.3181. Absorbance/emission (CH<sub>2</sub>Cl<sub>2</sub>): 1026, 1054 nm.

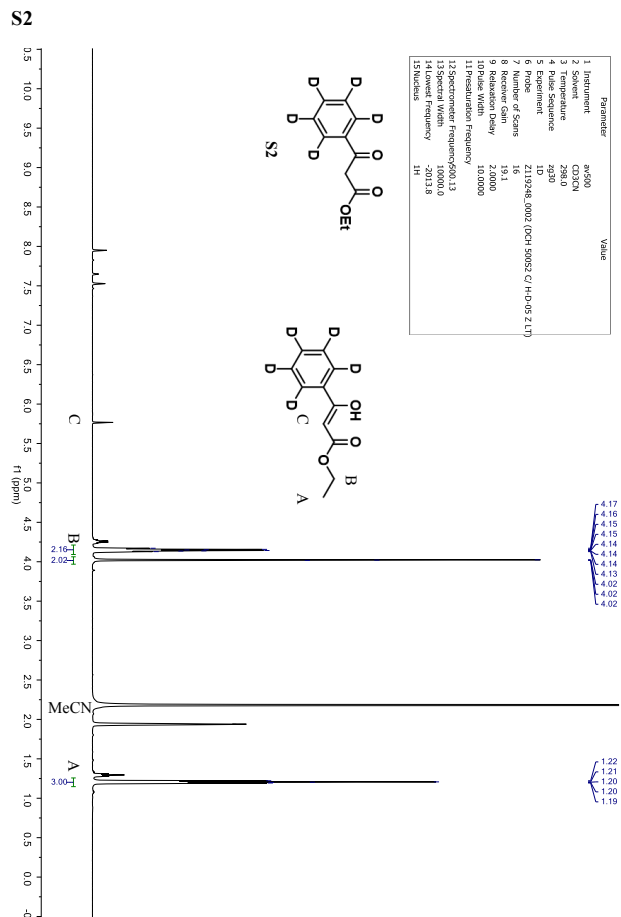


#### IV. <sup>1</sup>HNMR SPECTRA.

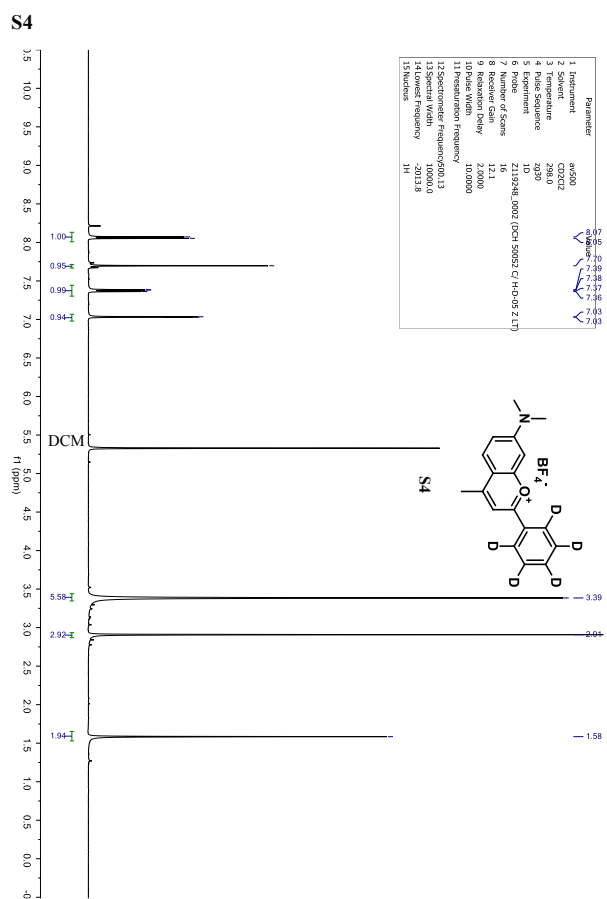
SH - 1

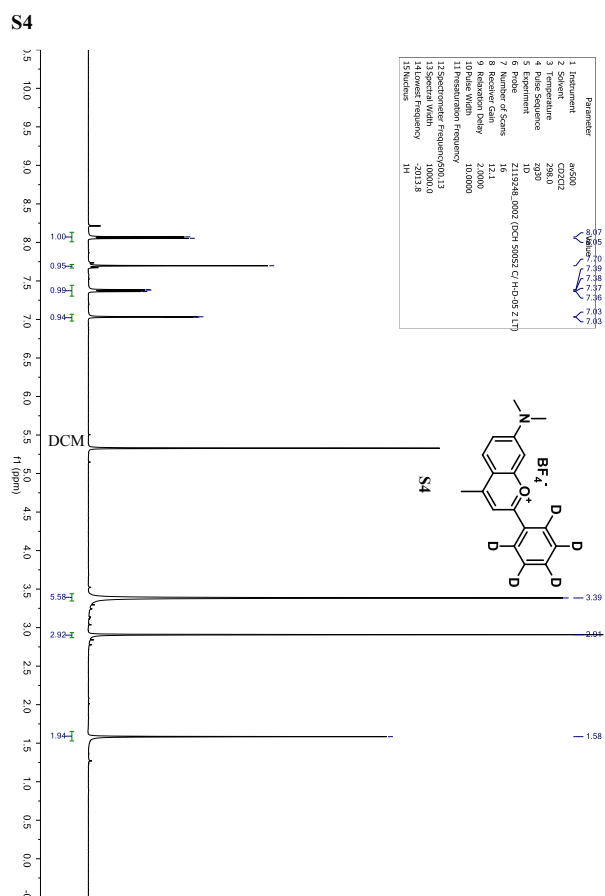
<sup>1</sup>H NMR Spectra.









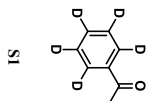
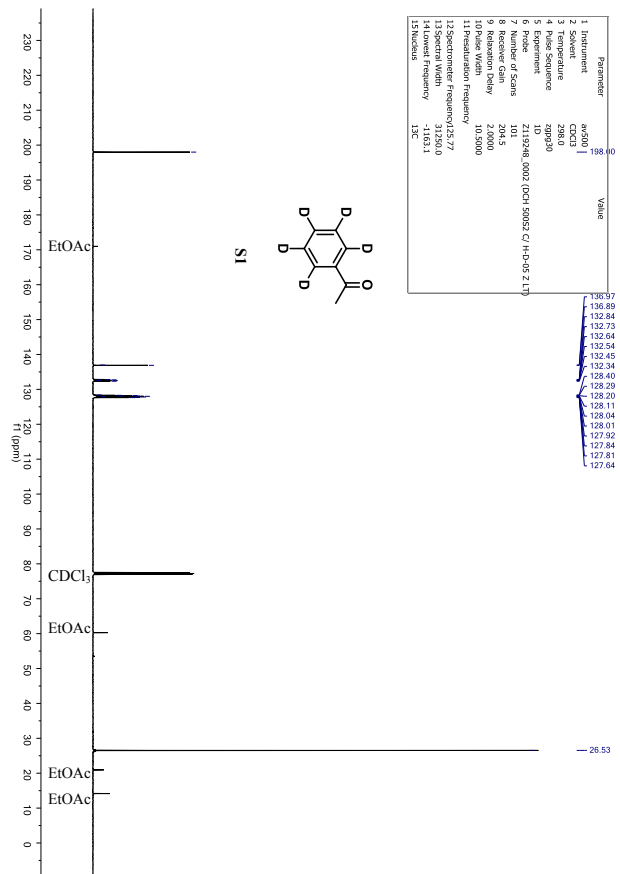


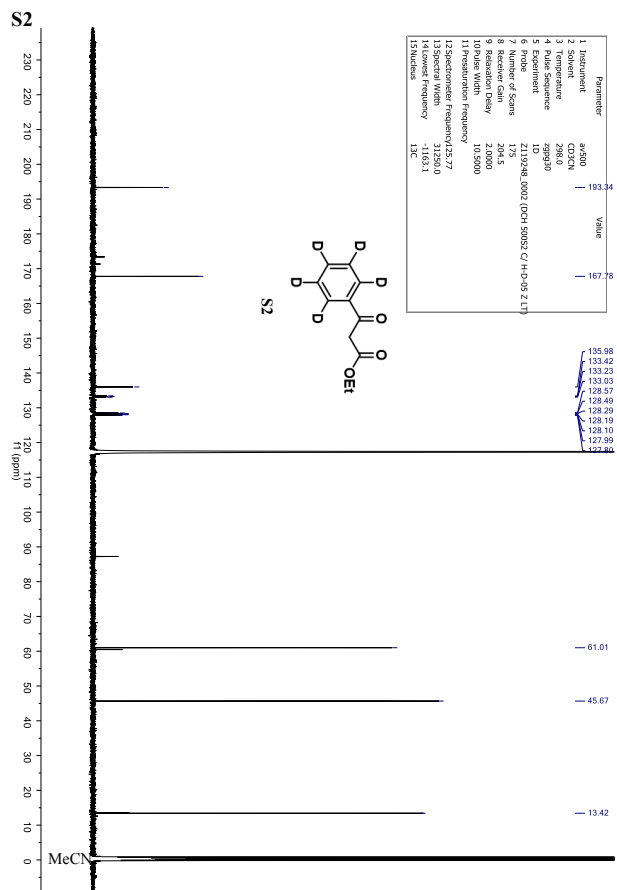
## V. $^{13}\text{C}$ NMR SPECTRA.

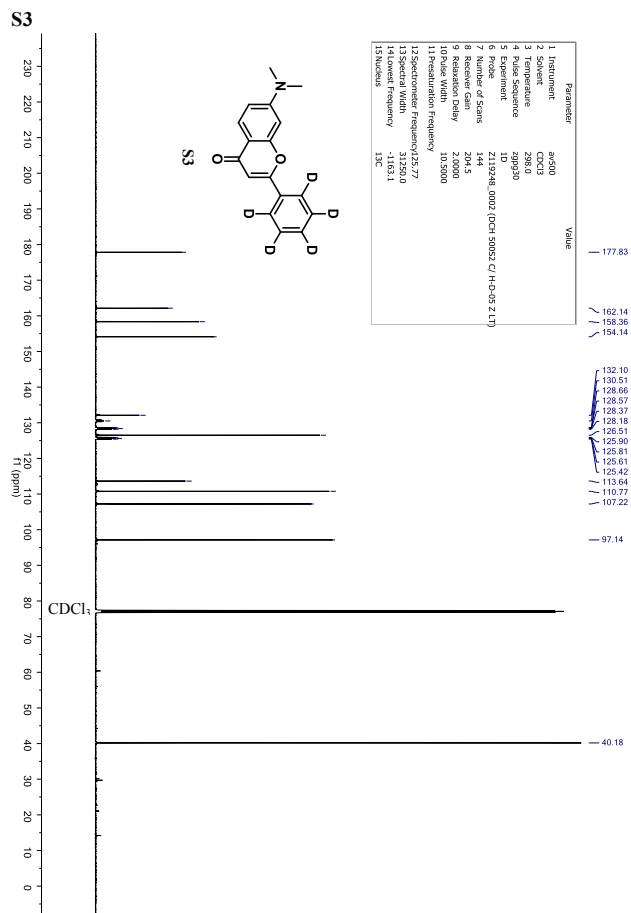
SC – 1

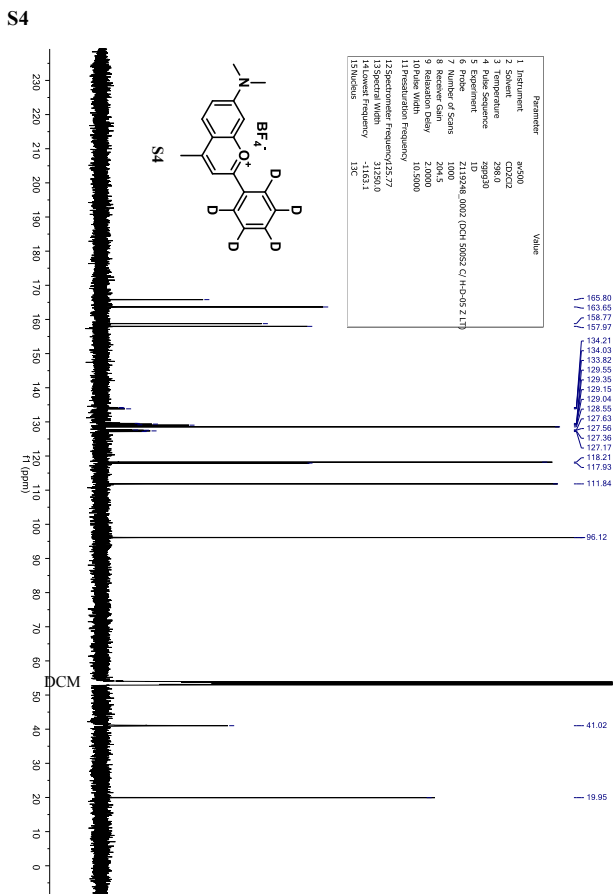
<sup>13</sup>C NMR Spectra

S1

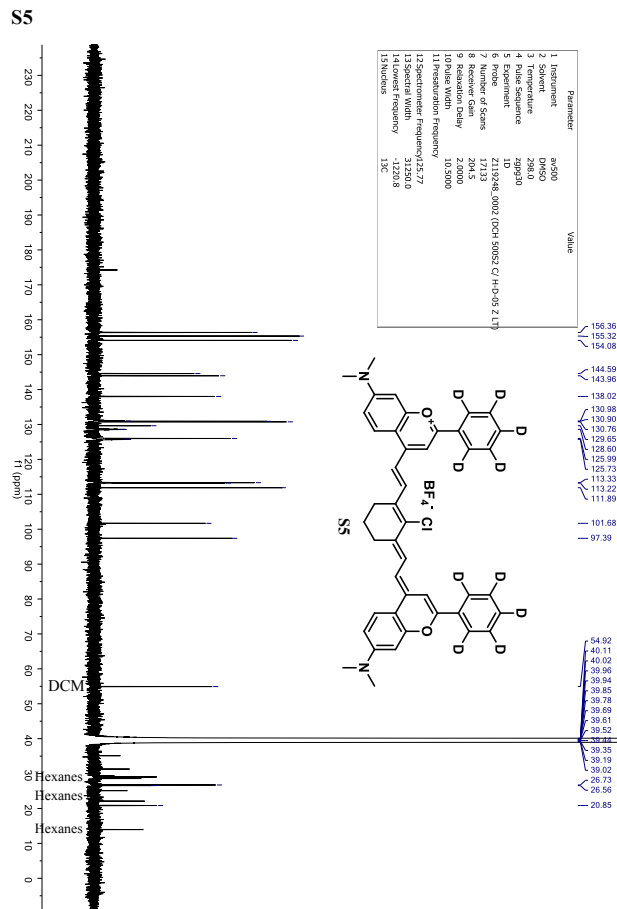












- <sup>1</sup>Frisch, M. J.; Trucks, G. W.; Schlegel, H. B.; Scuseria, G. E.; Robb, M. A.; Cheeseman, J. R.; Scalmani, G.; Barone, V.; Petersson, G. A.; Nakatsuji, H. et al. Gaussian 16 Revision C.01. 2016; Gaussian Inc. Wallingford CT.
- <sup>2</sup>Shao, Y.; Gan, Z.; Epifanovsky, E.; Gilbert, A. T.; Wormit, M.; Kussmann, J.; Lange, A. W.; Behn, A.; Deng, J.; Feng, X. et al. Advances in molecular quantum chemistry contained in the Q-Chem 4 program package. *Mol. Phys.* **2015**, *113*, 184–215.
- <sup>3</sup>Mennucci, B., Ed. *Continuum Solvation Models in Chemical Physics: From Theory to Applications*; Wiley: New York, 2007.
- <sup>4</sup>Jang, S. J. *Quantum Mechanics for Chemistry*; Springer Nature: New York, 2023.
- <sup>5</sup>Jang, S. “Nonadiabatic quantum Liouville equation and master equations in the adiabatic basis”. *J. Chem. Phys.* **2012**, *137*, 22A536.
- <sup>6</sup>Hellmann, H. *Einführung in die Quantenchemie*; Franz Deuticke: Leipzig, 1993.
- <sup>7</sup>Feynman, R. P. Forces in molecules. *Phys. Rev.* **1939**, *56*, 340–343.
- <sup>8</sup>Fatehi, S.; Alguire, E.; Shao, Y.; Subotnik, J. E. Analytic derivative couplings between configuration-interaction-singles states with built-in electron-translation factors for translational invariance. *J. Chem. Phys.* **2011**, *135*, 234105.
- <sup>9</sup>Ou, Q.; Bellchambers, G. D.; Furche, F.; Subotnik, J. E. First-order derivative couplings between excited states from adiabatic TDDFT response theory. *J. Chem. Phys.* **2015**, *142*, 064114.
- <sup>10</sup>Niu, Y.; Peng, Q.; Deng, C.; Gao, X.; Shuai, Z. Theory of excited state decays and optical spectra: Application to polyatomic molecules. *J. Phys. Chem. A* **2010**, *114*, 7817–7831.

- <sup>11</sup>Chang, J.-L. A new method to calculate Franck–Condon factors of multidimensional harmonic oscillators including the Duschinsky effect. *J. Chem. Phys.* **2008**, *128*, 174111.
- <sup>12</sup>Ruhoff, P. T.; Ratner, M. A. Algorithms for computing Franck–Condon overlap integrals. *Int. J. Quantum Chem.* **2000**, *77*, 383–392.
- <sup>13</sup>Eckart, C. Some studies concerning rotating axes and polyatomic molecules. *Phys. Rev.* **1935**, *47*, 552–558.
- <sup>14</sup>E. B. Wilson, J.; Decius, J. C.; Cross, P. C. *Molecular Vibrations: The theory of infrared and Raman vibrational spectra*; Dover Publications, Inc.: New York, 1955.
- <sup>15</sup>Marian, C. M. Spin-orbit coupling and intersystem crossing in molecules. *WIREs: Computational Molecular Science* **2011**, *2*, 187–203.
- <sup>16</sup>Pellegrini, C.; Müller, T.; Dewhurst, J. K.; Sharma, S.; Sanna, A.; Gross, E. K. U. Density functional theory of magnetic dipolar interactions. *Phys. Rev. B* **2020**, *101*.
- <sup>17</sup>Hirata, S.; Head-Gordon, M. Time-dependent density functional theory within the Tamm-Dancoff approximation. *Chem. Phys. Lett.* **1999**, *314*, 291–299.
- <sup>18</sup>Bellonzi, N.; Medders, G. R.; Epifanovsky, E.; Subotnik, J. E. Configuration interaction singles with spin-orbit coupling: Constructing spin-adiabatic states and their analytical nuclear gradients. *The Journal of Chemical Physics* **2019**, *150*, 014106.
- <sup>19</sup>Zhang, X.; Herbert, J. M. Analytic derivative couplings for spin-flip configuration interaction singles and spin-flip time-dependent density functional theory. *The Journal of Chemical Physics* **2014**, *141*, 064104.
- <sup>20</sup>Atallah, T. L.; A. V. Sica, A. V.; Shin, A. J.; H. C. Friedman, H. C.; Kahrobai, Y. K.; Caram, J. R. Decay-associated Fourier spectroscopy: Visible to shortwave infrared time-resolved photoluminescence spectra. *J. Phys. Chem. A* **2019**, *123*, 6792–6798.
- <sup>21</sup>Cosco, E. D.; Arús, B. A.; Spearman, A. L.; Atallah, T. L.; Lim, I.; Leland, O. S.; Caram, J. R.; Bruns, T. S. B. O. T.; Sletten, E. M. Bright chromenylium polymethine dyes enable fast, four-color in vivo imaging with shortwave infrared detection. *J. Phys. Chem. B* **2021**, *143*, 6836–6846.
- <sup>22</sup>Pengshung, M.; Neal, P.; Atallah, T. L.; Kwon, J.; Caram, J. R.; Lopez, S. A.; Sletten, E. M. Silicon incorporation in polymethine dyes. *Chem. Commun.* **2020**, *56*, 6110–6113.
-